J. Fluid Mech. (1992), *vol.* 243, *pp.* 353–392
Printed in Great Britain

The three-dimensional structure of periodic vorticity layers under non-symmetric conditions

By OMAR M. KNIO† AND AHMED F. GHONIEM
Department of Mechanical Engineering, Massachusetts Institute of Technology, Cambridge, MA 02139, USA

(Received 20 July 1990 and in revised form 27 March 1992)

Numerical simulations of a three-dimensional temporally growing shear layer are obtained at high Reynolds number and zero Froude number using a vortex scheme modified for a variable-density flow. Attention is focused on the effect of initial vorticity and density distributions on the interaction between instability modes which lead to the generation and intensification of streamwise vorticity. Results show that the three-dimensional instabilities evolve following the formation of concentrated spanwise vorticity *cores*. The deformation of each core along its span resembles the amplification of the translative instability. The generation of vortex *rods*, which wrap around individual cores while stretching between neighbouring cores, suggest a mode similar to the Corcos instability. The instability modes leading to the formation of both structures, energized by the extensional strain generated by the cores, grow simultaneously. A similar series of events occurs in variable-density shear layers and in shear layers which start with an asymmetric vorticity distribution. Baroclinic vorticity generation in the variable-density layer leads to the formation of asymmetric cores whose volumetric composition is biased towards the lighter fluid. The structures are propelled, by their asymmetric vorticity distribution, in the direction of the heavier stream while their eccentric spinning forces an uneven stretching of the vortex rods. The origin of the asymmetry is established by comparing these with the results of a shear layer with an initially asymmetric vorticity distribution in a uniform-density flow. The strong late-stage asymmetry exhibited by the former is not observed in the latter. Thus, baroclinic vorticity generation is responsible for the observed symmetry. We also find that initially asymmetric vorticity distribution does not, as suggested before, lead to asymmetric spacing between the streamwise rods. it is concluded that the experimentally observed asymmetric spacing must arise after pairing.

1. Introduction

The formation of large vortical structures has long been observed in free shear layers at high Reynolds numbers (Crow & Champagne 1970; Brown & Roshko 1974). Analysis of experimental results shows that the evolution of these structures and their mutual interactions, governed essentially by inviscid flow dynamics, play an important role in the growth of the layer, the distribution of turbulent statistics, scalar transport and mixing (Winant & Browand 1974; Ho & Huerre 1984; Dimotakis 1989; Hussain 1986). Without external forcing, the early stages of the

† Present address: Department of Mechanical Engineering, The Johns Hopkins University, Baltimore, MD 21218, USA.

layer are dominated by two-dimensional motion, where spanwise vortex structures are formed, followed by a transition to three-dimensional motion. Within and after the transition region, the spanwise vortices are deformed, and secondary streamwise vortices are generated (Konrad 1976; Breidenthal 1981; Jimenez 1983; Bernal 1981). Experimental investigations yielded striking visualizations of the streamwise structures, and how they modify scalar transport (Jimenez, Cogollos & Bernal 1985; Bernal & Roshko 1986). In recent work, Lasheras, Cho & Maxworthy (1986) and Lasheras & Choi (1988) examined the possibility of manipulating the location of the 'transition' region by three-dimensional forcing (see also Breidenthal 1980), thereby emphasizing the practical aspect of such studies.

The three-dimensional response of vorticity layers is complex and determining the origin and shape of the secondary structures poses considerable difficulties to analytical studies. So far, a limited number of theoretical investigations have dealt with this problem. Pierrehumbert & Widnall (1982) used a periodic array of Stuart vortices to represent the spanwise eddies formed by the roll-up of the Kelvin–Helmholtz instability. The linear stability analysis of this configuration revealed the presence of a 'translative' instability, which was then proposed as a possible mechanism leading to the formation of the observed secondary vortices in shear layers. Another mechanism, discovered by Corcos & Lin (1984) in their study of the stability of the layer by linearizing three-dimensional perturbations around the evolving two-dimensional flow (Lin & Corcos 1984), was also suggested. They showed that, for sufficiently low diffusion (Neu 1984), the strained streamwise vorticity is unstable, and the instability causes the redistribution of the latter into round, concentrated vortex rods. These streamwise rods lead to the generation of 'mushroom' structures similar to those experimentally observed (Bernal & Roshko 1986; Lasheras *et al.* 1986; Lasheras & Choi 1988). Manifestation of both instability mechanisms has been reported in experimental studies; however, the broadband nature of the three-dimensional modes predicted in both theories complicates the task of verifying their validity or determining flow conditions under which one mode dominates the other.

The three-dimensional motion of shear layers has also been the subject of numerical investigations. Ashurst & Meiburg (1988) used a vortex filament scheme to compute the development of a temporal shear layer at high Reynolds number. The shear layer was modelled by a single desingularized vortex sheet or two vortex sheets of opposite sign. Results of both models showed evidence of both the translative and the Corcos instability modes. When two sheets of opposite sign were used, an asymmetric distribution of streamwise vortices (Lasheras & Choi 1988), was apparently reached through a nonlinear interaction between two counter-rotating streamwise vortex rods, each originating in a distinct vorticity layer. While a similar asymmetric distribution of vortices was observed experimentally in shear layers, the initial vorticity profile used in this simulation was more representative of that of a wake. The difference between the stability and long-time behaviour of wakes and shear layers would be seen by comparing the results of Ashurst & Meiburg and of Grinstein, Hussain & Oran (1989), who used a finite-difference scheme to simulate the evolution of a spatially developing shear layer at moderate Reynolds number. Results of the latter indicate that the asymmetric distribution of streamwise vortices develops as a result of the merging of pairs of streamwise rods of the same sign of circulation, and that this interaction only occurs after pairing between neighbouring spanwise eddies.

The 'sequential' nature of the growth of several forms of two- and three-

dimensional instabilities was investigated in the spectral calculations of Metcalfe *et al.* (1987). They considered temporal vorticity layers at low Reynolds number, and performed a detailed study of the energy content of the distinct modes. Their results show that, for small perturbations, two-dimensional Kelvin–Helmholtz waves grow first. During their growth, three-dimensional activity is suppressed and the layer maintains a two-dimensional character. Following the nonlinear growth of the Kelvin–Helmholtz waves and the formation of ('primary') spanwise eddies, three-dimensional perturbations are amplified. Saturation of the Kelvin–Helmholtz and three-dimensional instabilities is reached soon after the flattening of the (primary) spanwise cores and the 'maturation' of three-dimensional modes. They also show that pairing of spanwise cores, during which three-dimensional activity is suppressed, is necessary for further growth of the layer. Following pairing, the growth of three-dimensional modes is resumed. Amplification of three-dimensional disturbances is thus restricted to windows separating periods of otherwise two-dimensional growth.

The dependence of the response of the shear layer on initial conditions and forcing levels was investigated by Inoue (1989), who performed a vortex filament simulation of a spatially developing layer modelled by a single vortex sheet. His results show that the three-dimensional transition strongly depends on three-dimensional forcing, and that the flow field tends towards two-dimensional behaviour once this forcing is interrupted. This was contradicted by the numerical experiments of Grinstein *et al.* (1989) which indicate that the transition to three-dimensional motion persists despite the absence of a continuous forcing function. This result was verified in the simulations of Lowery, Reynolds & Mansour (1987), who employed a hybrid finite difference – spectral method to track the evolution of a passive scalar in a developing layer at low Reynolds number. While the study focused on asymmetric entrainment patterns in two and three dimensions (Dimotakis 1989, 1986), it also emphasized the fact that distributions of spanwise and streamwise vorticity are weakly dependent on the strength and shape of the forcing function. As indicated below, vortex simulations, similar to those of Inoue (1989) and Ashurst & Meiburg (1988), which do not allow the number of computational elements to increase as the material elements are stretched, may lose accuracy and contaminate the computations with numerical diffusion errors.

Despite these efforts, a clear and unified interpretation of the role of the various modes in the formation of vortical and scalar structures, a crucial step towards a better understanding of three-dimensional transition, has not been reached. Moreover, several important issues, summarized next, cast some doubt on the conclusions of these simulations. Using desingularized vortex sheets to model shear layers, as in Ashurst & Meiburg (1989), may lead to spurious results since, as shown by the detailed numerical study of Knio & Ghoniem (1991), the properties of the three-dimensional modes of a vortex structure are strongly dependent on the vorticity distribution within the cross-section of the structure. The use of vortex filaments to resolve vorticity within the shear layer is not recommended since the corresponding schemes, although accurate for short times, do not maintain their accuracy as vortex elements tend to move apart due to stretching in the direction normal to that of the main flow. This violates an important accuracy condition in vortex methods, namely that the cores of neighbouring vortex elements must, at all times, overlap.

Another source of inaccuracy in the simulations presented in Ashurst & Meiburg (1988) is the enforcement of the periodic boundary conditions. A small number of images was used on either side of the computational domain, which was not enough

to capture the correct value of the free-stream velocity. On the other hand, the conclusions of the spectral simulations of Metcalfe *et al.* (1987), particularly those concerning the onset of and the interaction between the two- and three-dimensional modes described above, may be dependent on some diffusive–convective balance achieved only at low Reynolds number. This balance, which is a function of the Reynolds number, can lead to an early saturation of the instability. We believe that a high-Reynolds-number simulation is necessary to determine whether the interaction between the different modes of the three-dimensional instability is, as widely suspected, an essentially inviscid mechanism.

The large number of mechanisms governing the evolution of shear layers, and the complexity of the resulting vortical and scalar structures underscore the need for accurate numerical methods which can carefully treat the vorticity transport equation. Successful implementation of numerical schemes depends on the proper account of the vorticity stretching term, and, if present, vorticity source terms. Another crucial ingredient lies in the ability of the method to accommodate the large strain associated with high concentrations of vorticity. The latter have been shown to result in the deterioration of the discretization accuracy in both Eulerian computations, through the creation of small-scale structures which may not be well represented on a grid of fixed mesh size and the accumulation of numerical diffusion which may dissipate these structures at their early stages, and Lagrangian computations where zones of high strain may be depleted of computational elements. Finally, questions regarding the dynamic effect of density gradients, in the absence of gravity, which impact mixing of gases at different molecular weight and/or density, have not been tackled before.

In this work, an adaptive, Lagrangian numerical scheme is used in the simulation of vorticity layers. Two main ingredients are incorporated in the construction of the scheme, which was analysed in our previous effort (Knio & Ghoniem 1991). The first relates to its adaptive nature, a feature which avoids the loss of spatial resolution and allows the accommodation of high strain rates by increasing the number of computational elements as the flow evolves. The second, a property found in most Lagrangian methods, consists of ensuring a minimal effect of numerical diffusion which may lead to excessive smearing of the vorticity. We also apply a vortex scheme extended to variable-density flows to analyse the dynamic effect of finite density gradients on the evolution of the shear layer.

Computed results are used to accurately portray the severe deformation of the flow map and the evolution of the flow vorticity. We focus on the relationship between the deformation of material surfaces, the generation and intensitification of vorticity and the associated scalar entrainment patterns. The results are used to characterize the three-dimensional instabilities of the vorticity layer. Instability modes leading to the generation of streamwise vortex rods joining neighbouring eddies are identified and distinguished from those affecting the vortex cores. A generalized perspective of the latter is given; the similarity between vorticity patterns found in the late stages of spanwise vortex cores in the shear layer and those observed in the development of vortex rings is discussed. Finally, we investigate some of the mechanisms leading to the onset of asymmetry in an otherwise symmetric flow. In particular, a variable-density layer is contrasted with a uniform-density asymmetric layer, in order to study the roles of density variation and asymmetric strain field on the development of the vorticity field.

The numerical scheme used in the computations is summarized in §2. In §3 we review the evolution of a uniform-density symmetric layer, then present results of

variable-density and asymmetric vorticity layer computations. The results are further discussed in §4; concluding remarks are given in §5.

2. Formulation and numerical scheme

2.1. *Formulation and governing equations*

We start with the incompressible, isentropic, variable-density form of the governing equations in the low-Mach-number limit (Rehm & Baum 1978; Majda & Sethian 1987; Ghoniem & Krishnan 1989). By choosing an appropriate combination of characteristic length, time and velocity scales as normalizing parameters, these equations are written as

$$\frac{\mathrm{D}\rho}{\mathrm{D}t} = 0, \tag{1}$$

$$\rho \frac{\mathrm{D}\boldsymbol{u}}{\mathrm{D}t} = -\nabla p, \tag{2}$$

where $\boldsymbol{x} = (x, y, z)$ is the position vector, $\boldsymbol{u} = (u, v, w)$ is the velocity, t is time, $\nabla = (\partial/\partial x, \partial/\partial y, \partial/\partial z)$ is the gradient operator, and $\mathrm{D}/\mathrm{D}t = \partial/\partial t + \boldsymbol{u}\cdot\nabla\boldsymbol{u}$ is the material derivative. Since the pressure and density variations are decoupled, we can supplement (1) and (2) with

$$\nabla\cdot\boldsymbol{u} = 0. \tag{3}$$

By taking the curl of (2) and using the solenoidality condition, (3), we get the vorticity transport equation:

$$\frac{\mathrm{D}\boldsymbol{\omega}}{\mathrm{D}t} = \boldsymbol{\omega}\cdot\nabla\boldsymbol{u} + \frac{\nabla\rho}{\rho^2}\times\nabla p, \tag{4}$$

where $\boldsymbol{\omega} = \nabla\times\boldsymbol{u}$ is vorticity. A more suitable form of the vorticity transport equation is derived by substituting (2) for ∇p into (4), thus yielding

$$\frac{\mathrm{D}\boldsymbol{\omega}}{\mathrm{D}t} = \boldsymbol{\omega}\cdot\nabla\boldsymbol{u} - \frac{\nabla\rho}{\rho}\times\frac{\mathrm{D}\boldsymbol{u}}{\mathrm{D}t}. \tag{5}$$

The vorticity associated with a material particle changes due to tilting and stretching under the action of the strain, $\nabla\boldsymbol{u}$, and due to the particle acceleration in a non-uniform density field. Equation (5) is preferred over (4) because the baroclinic source term is written in terms of the kinematics of the flow field rather than being treated as a dynamic effect associated with pressure forces. Buoyancy effects have been neglected in the vorticity transport equation since we intend to focus on high-speed flows in which fluid acceleration is much larger than gravitational acceleration. Under these conditions, gravity effects are negligible whenever the Richardson number,

$$Ri = \frac{g\Delta\rho\,\Delta l}{\rho_o U^2} \tag{6}$$

written in terms of the gravity constant, g, and characteristic density ρ_0, length Δl, density difference $\Delta\rho$, and velocity difference U, is small (Koop & Browand 1979).

The presence of the baroclinic source term requires the accurate estimation of the density gradient. To this end, we derive a transport equation for the scalar gradient (the density in this case), by taking the gradient of (1) to obtain

$$\frac{\mathrm{D}\boldsymbol{g}}{\mathrm{D}t} = -\boldsymbol{g}\cdot\nabla\boldsymbol{u} - \boldsymbol{g}\times\boldsymbol{\omega}, \tag{7}$$

where $\boldsymbol{g} = \nabla\rho$. Thus, while density remains constant along a material path, its gradient is affected by the local strain and the vorticity. Working with (7) instead of (1) is similar to using the vorticity transport equation in place of the momentum equation. Both substitutions are motivated by the observation that, in most high-Reynolds-number flows, the supports of the vorticity and scalar gradient are small subsets of the supports of the primitive variables. Thus, computational effort is concentrated into smaller regions of the domain of study, and the numerical differentiation of the density field is avoided, thereby minimizing a loss of resolution.

2.2. *Numerical scheme*

The transport element method is used to compute the evolution of the shear layer. The numerical scheme solves the time-dependent, inviscid, incompressible, vorticity, scalar and scalar gradient transport equations given above. Variants of the numerical scheme which accommodate gravity, compressibility, chemical reactions and diffusion have been extensively used in two dimensions (Ghoniem & Krishnan 1988), and in a limited number of applications in three-dimensions (Knio & Ghoniem 1992), but will not be required in this study.

The numerical method is the product of the combination of a series of refinements of three-dimensional vortex methods with the scalar transport techniques developed in the two-dimensional transport element method (Ghoniem, Heidarinejad & Krishnan 1988). It is based on the discretization of the vorticity and scalar gradient fields into a finite number of Lagrangian elements, called transport elements. Transport elements carry discrete scalar, vorticity and scalar gradient values, and are distributed along elementary rectangular areas which are used to divide entire material surfaces. The Lagrangian mesh defines the location of the elements, while vector quantities are not restricted to lie within elementary rectangular areas. Discrete quantities are smoothed in a small spherical neighbourhood of the centre of the element. A third-order Gaussian core function, $\psi_\delta = 3/(4\pi\delta^3)\exp(-r^3/\delta^3)$, is used as smoothing function, and its standard deviation δ is used as characteristic core radius (Knio & Ghoniem 1991). This yields a continuous version of the vorticity field which induces a desingularized velocity field, expressed in terms of the Biot–Savart law (Batchelor 1967). The material surfaces are tracked by moving the vertices of the elements with the local velocity vector, using a second-order, predictor–corrector time-integration scheme.

The construction of the transport element method closely mimics conventional vortex elements schemes. Numerical analysis of these schemes reveals that the smoothing functions control the order of the spatial resolution and that strong overlap among the cores of neighbouring elements is required to guarantee convergence (Beale & Majda 1982*a*, *b*; Beale 1986). While the third-order Gaussian functions have been shown to yield second-order schemes (Leonard 1985; Beale & Majda 1985), it is the overlap condition that first motivated the modification of the three-dimensional vortex method, in which vortex elements are distributed along vortex tubes. In vortex methods and vortex filament methods, vortex elements are redistributed along vortex tubes whenever the strain causes the separation distance between neighbouring elements to exceed the core radius. However, the overlap condition cannot be enforced if the elements (or filaments) are strained in a direction normal to the local vorticity vector. As a result, deterioration in the spatial resolution may occur at long times as large discretization errors pollute the solution. In the present computations, a scheme of local mesh refinement which subdivides computational elements along two directions of strain is employed. This scheme,

which is described below, has been shown to yield significant improvement in the accuracy of the computations over vortex element computations (Knio & Ghoniem 1991).

Another advantage of the transport element method lies in the fact that tracking material surfaces greatly simplifies the task of integrating the equation of motion of the density gradient. This is achieved by associating which each transport element an elementary surface area $\delta \boldsymbol{A}_i(t)$ and a unit normal to the surface areas at the centre of the element $\boldsymbol{n}_i(t) = \delta \boldsymbol{A}_i(t)/|\delta \boldsymbol{A}_i(t)|$. In the computations, this is done by requiring that material surfaces effectively constitute iso-scalar surfaces, and adopting linear interpolation functions to describe the shape of the material surface within each transport element. We take advantage of kinematical relationships which relate the evolution of the gradient of a non-diffusive scalar in an incompressible fluid at a material point $\chi(t), \boldsymbol{g}(t, \chi)$, to that of an elementary surface area centred around $\chi, \delta \boldsymbol{A}(t, \chi)$, initially having the same sense and direction as $\boldsymbol{g}$. This relationship, which constitutes the analogue of the Helmholtz vorticity theorem, may be expressed as: $\boldsymbol{g}(t, \chi) = \alpha \delta \boldsymbol{A}(t, \chi)$, where $\alpha = |\boldsymbol{g}(0, \chi)|/|\delta \boldsymbol{A}(0, \chi)|$. In view of the preceding, we avoid integrating (7) simply by following the evolution the elementary surface areas.

The description of the method is completed by specifying a technique for updating the discrete values of vorticity associated with the transport elements. Two techniques are used in the computations. In the absence of density variation, direct integration of the vorticity transport equation is avoided. In this case, substantial computational savings are achieved by taking advantage of the Helmholtz and Kelvin theorems since vorticity lines, identified by their circulation, evolve as material lines. In this variant of the scheme, vorticity changes according to the stretching and tilting of elementary material segments lying in its direction, while the circulation associated with a transport element remains constant. This procedure avoids the evaluation of the velocity gradient, and retains the property of the conservation of the volume of vorticity possessed by vortex filament methods (Greengard 1986).

When dealing with variable-density flows, we can no longer apply the Helmholtz vorticity theorem. Therefore, we are not able to avoid the integration of (5), and, in doing so, the evaluation of the velocity gradient. The procedure suggested here is to split that task in two fractional steps, by first numerically integrating

$$\frac{\mathrm{D}\boldsymbol{\omega}}{\mathrm{D}t} = \boldsymbol{\omega} \cdot \nabla \boldsymbol{u} \tag{8}$$

and, in a second step, integrating

$$\frac{\mathrm{D}\boldsymbol{\omega}}{\mathrm{D}t} = -\frac{\nabla \rho}{\rho} \times \frac{\mathrm{D}\boldsymbol{u}}{\mathrm{D}t}. \tag{9}$$

This procedure is similar to the 'viscous splitting' of the viscous vorticity transport equation (Chorin 1973), and thus may be termed 'baroclinic splitting' of the equation of motion. In the numerical integration of (8), $\nabla \boldsymbol{u}$ is found by analytically differentiating the desingularized Biot–Savart law, while the same predictor–corrector employed to advance the computational mesh is used to perform the time integration. Equation (9) is integrated in a single step, by estimating the baroclinic torque from knowledge of (i) ρ, which is constant for each element; (ii) $\nabla \rho$, which is computed according to the deformation of the elements; and (ii) $\mathrm{D}\boldsymbol{u}/\mathrm{D}t$, which is approximated by a first-order, backward finite difference in time, $\mathrm{D}\boldsymbol{u}/\mathrm{D}t \approx (\boldsymbol{u}(t) - \boldsymbol{u}(t - \Delta t))/\Delta t$.

In the nonlinear evolution of the flow field, a strong and rapid deformation of the Lagrangian computational mesh is experienced. This deformation causes the depletion of computational elements in some regions of the domain where the separation distance between neighbouring elements becomes excessively large. In this work, we employ a local mesh refinement scheme which splits a transport element into two whenever the average value of opposing sides of the rectangles exceeds the value of the core radius. The scheme has been described in detail in Knio & Ghoniem (1991). It essentially ensures that core overlap among neighbouring elements is satisfied and amounts to redistributing the vorticity and scalar fields into a larger number of elements due to strong strain.

2.3. *Initial and boundary conditions*

A variable-density temporal vorticity layer of finite thickness is assumed at $t = 0$. A right-handed rectangular coordinate system (x, y, z) is chosen so that the initial vorticity distribution is aligned with the positive y-axis, the flow being uniform in the streamwise x-direction. A second-order Gaussian vorticity distribution with standard deviation σ is adopted to describe the variation of vorticity within the layer. The thickness of the vorticity layer, σ, and the free-stream velocity are chosen as length and velocity scales. The initial vorticity and velocity field are given, respectively, by $\omega_y(\boldsymbol{x}, 0) = 2/(\sigma\pi)^{\frac{1}{2}} \exp(-z^2/\sigma^2)$, $\omega_x(\boldsymbol{x}, 0) = \omega_y(\boldsymbol{x}, 0) = 0$, $v(\boldsymbol{x}, 0) = \mathrm{erf}(z/\sigma)$, $v(\boldsymbol{x}, 0) = w(\boldsymbol{x}, 0) = 0$. For $\sigma = 1$, the velocity initial flow field satisfies: $u(z \to \pm\infty) = \pm 1$. Furthermore, the layer is assumed periodic in the streamwise x- and spanwise y-directions, with periodicity lengths λ_x and λ_y respectively, and is unbounded in the cross-stream z-direction. The initial density distribution is an error-function profile, and the reference density scale is chosen so that the low-density fluid has $\rho = 1$.

The periodicity boundary conditions introduce some difficulties in the evaluation of the flow field and of its gradient since we must consider the image system of the transport elements. This system yields an additional term which must be added to the velocity induced by the elements in the domain. Unlike the two-dimensional case, this term must not be deduced from a potential flow, and closed-form expressions to its effect are not known (Ashurst & Meiburg 1988). In the computations, we have adopted the procedure described in Knio & Ghoniem (1991), which consists of computing directly the effect of the eight immediate neighbours of the elements and approximating the induced velocity of the images which lie within a square of side $400\lambda_x$ by interpolation on a fixed grid. While previous studies have only included the contribution of a small number of images (Ashurst & Meiburg 1988), the procedure suggested in Knio & Ghoniem (1991) is preferred because it yields more accurate representations of the velocity and velocity gradient fields, and avoids the generation of numerical boundary layers at the spanwise boundaries of the domain (Inoue 1989).

3. Results

In this section, we focus on the deformation of the primary (essentially two-dimensional) structure due to the three-dimensional instabilities, and on the formation of secondary structures as these instabilities evolve into their nonlinear stages. We attempt to unify the various postulates on the origin and mechanisms of the three-dimensional motion. By comparing our results to available experimental evidence (Breidenthal 1980, 1981; Jimenez 1983; Jiminez *et al.* 1985; Bernal 1981;

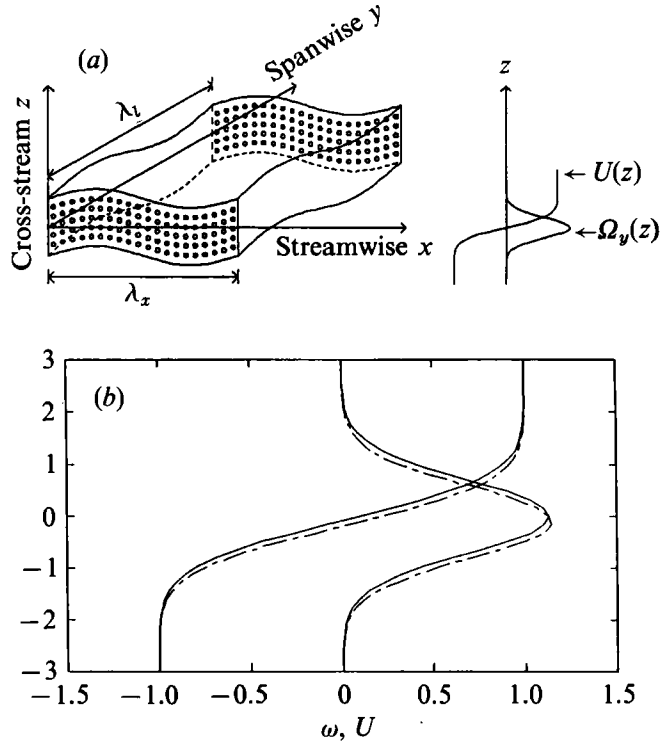

FIGURE 1. (*a*) Schematic representation of the shear layer, the coordinate axes, and the initial vorticity and scalar distributions, showing the shape of the perturbation, and the initial location of the vortex tubes. (*b*) Vorticity and velocity profiles for the symmetric and asymmetric layers discussed in §§3.1 and 3.3 respectively.

Lasheras & Choi 1988; Lasheras *et al.* 1986) and to numerical solutions (Ashurst & Meiburg 1988; Metcalfe *et al.* 1987; Lowery *et al.* 1987; Grinstein *et al.* 1989), we proceed to clarify some of the aforementioned issues, and point to strengths and deficiencies of previously proposed models. Another objective is to provide a base solution which, in turn, is used to highlight the baroclinic effects in the variable-density layer.

3.1. *Symmetric, uniform-density shear layer*

A temporal shear layer with streamwise periodicity length $\lambda_x = 13.2$, which matches the wavelength of the most unstable two-dimensional mode (Ghoniem & Krishnan 1988) and spanwise periodicity length $\lambda_y = \frac{1}{2}\lambda_x$, which lies close to the most amplified three-dimensional mode of the translative instability (Pierrehumbert & Widnall 1982), was computed. The initial scalar distribution has a zero mean and a unit difference across the layer. The shear layer is initially discretized among elements distributed on a grid of $20 \times 14 \times 5$ points along the x-, y-, and z-directions respectively. Thus, computational elements are distributed on five material or iso-scalar surfaces. The selection of the number of material surfaces is chosen as the minimum number required for accurate representation of the eigenfunctions of the Kelvin–Helmholtz instability (Ghoniem *et al.* 1988). The core radius of the smoothing functions is chosen so that strong overlap among the cores of neighbouring elements is ensured, and the vorticity of the elements is obtained by minimizing the integral error between assumed and discretized vorticity profiles (Knio & Ghoniem 1991). In the computations, we set $\delta = 0.89$ and the time step $\Delta t = 0.1$. The layer is initially

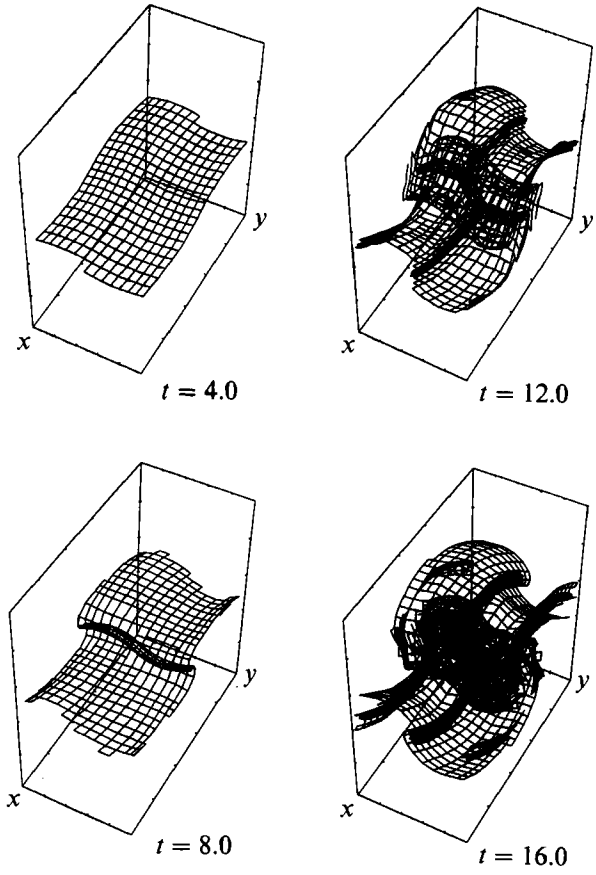

FIGURE 2. Three-dimensional perspective view of the surface $s = 0$, initially lying in the plane $z = 0$. The plots were generated from the point of view of an observer located at (48, 24, 48). x is the streamwise direction, y the spanwise direction, and z the cross-stream direction.

perturbed in both the streamwise and spanwise directions by displacing the computational elements in the cross-stream direction using sinewaves of amplitude $\epsilon = 0.02\lambda_x$, i.e. by using the transformation $z_i \rightarrow z_i + \epsilon \sin(2\pi x_i/\lambda_x) + \epsilon \sin(2\pi y_i/\lambda_y)$ (see figure 1.)

3.1.1. *Deformation of material surfaces*

Figures 2 and 3 depict perspective views of the iso-scalar surfaces initially located at $z = 0$, and -1.32 respectively. The surface initially lying at $z = 0$ represents the middle surface where most of the vorticity is concentrated, while increasing or decreasing the value of z corresponds to motion towards the top or bottom streams. The plots are generated from the point of view of an observer located at (48, 24, 48).

Owing to rollup of the layer, computational elements accumulate in the core which forms during $4.0 < t < 8.0$. Previous analysis of the two-dimensional solution indicates that, for the present amplitude of the streamwise perturbation, the linear stages of the evolution of the primary two-dimensional instability end between $t = 4.0$ and 8.0, followed by rollup. The amplitude of the spanwise perturbation remains small for $t < 8.0$, i.e. its amplification is essentially suppressed during the growth of the two-dimensional mode.

The growth of the eddy core in the mid-section of the domain continues while its spanwise waviness amplifies. The amplitude of the spanwise perturbation increases

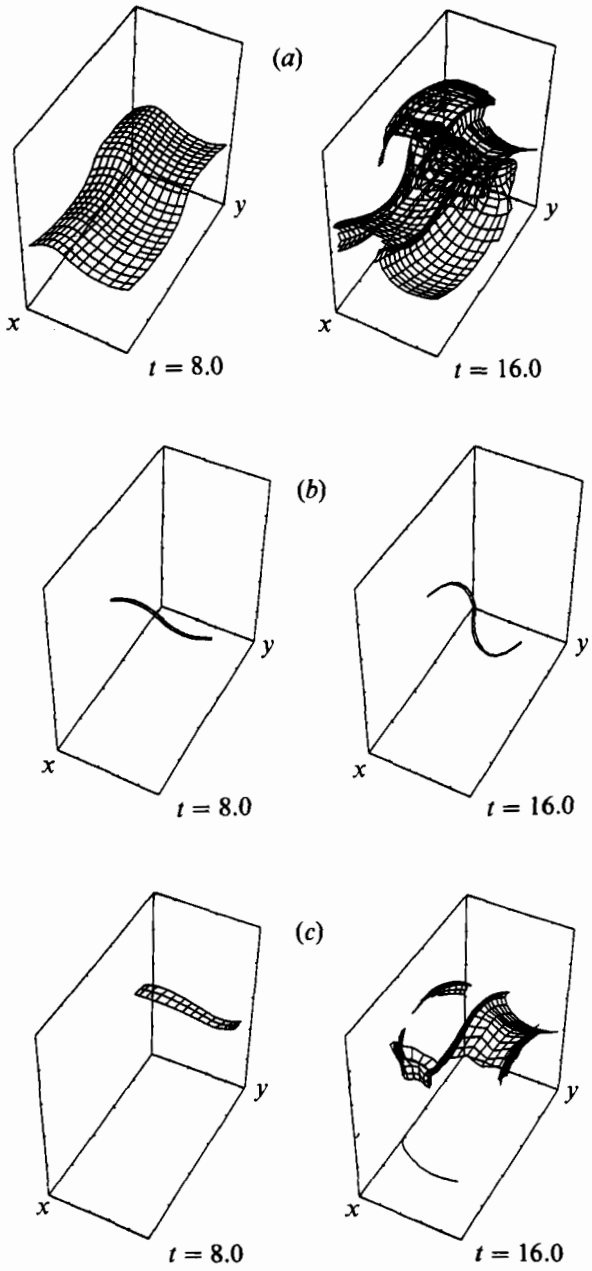

FIGURE 3. Three-dimensional perspective view of the iso-scalar surface (*a*) initially lying in the plane $z = -1.32$, (*b*) embedded in the middle layer and coinciding with the axis of the spanwise core, and (*c*) embedded in the middle layer and located within the braids. The plots are generated as in figure 2.

significantly along the core, an indication of the evolution of the translative instability (Pierrehumbert & Widnall 1982). This uneven axial displacement of the spanwise core is accompanied by an out-of phase deformation of the braids under the influence of the streamwise vorticity generated within the cores. The growth of the translative instability is shown in figure 3 (*b*) by plotting the row of elements initially aligned along the core centerline. Vortex lines aligned with the axis of the spanwise

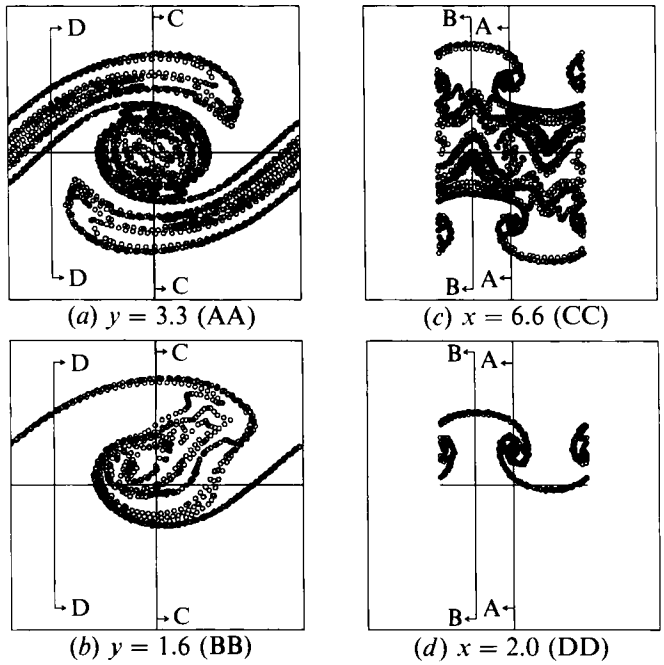

(a) $y = 3.3$ (AA) (c) $x = 6.6$ (CC)

(b) $y = 1.6$ (BB) (d) $x = 2.0$ (DD)

FIGURE 4. Intersection of the Lagrangian mesh at $t = 18.0$ with the planes (a) $y = 3.3$, (b) $y = 1.6$, (c) $x = 6.6$, and (d) $x = 2.0$. The intersection points are illustrated in terms of small circles whose radius is $\frac{1}{8}$ of the core radius of the transport elements.

Material layer	z location	$t = 4.0$		$t = 8.0$		$t = 12.0$		$t = 16.0$	
		A	N	A	N	A	N	A	N
1	−1.32	1.03	1.00	1.12	1.20	1.62	1.68	3.26	3.80
2	−0.66	1.04	1.00	1.22	1.33	2.31	2.54	4.79	7.05
3	0	1.04	1.00	1.43	1.49	2.71	3.24	5.41	9.53
4	0.66	1.04	1.00	1.22	1.33	2.31	2.54	4.79	7.05
5	1.32	1.03	1.00	1.12	1.20	1.62	1.68	3.26	3.80

TABLE 1. Normalized surface area, A, and number of elements, N, for the individual material layers

core suffer a mild net deformation in the streamwise direction. The evolution of the spanwise core instability occurs such that vortex lines constantly realign with the direction strain while being stretched along their axial direction.

The fluid motion along the braids is illustrated in figure 3(c). The stretching of the braids leads to the intensification of streamwise vorticity produced as the braids are deformed by the growth of the 'translative' instability along the core, and strained by the two-dimensional flow field. Vortex rods, which extend throughout the braids and are wrapped around the spanwise cores, form as streamwise vorticity rolls into coherent eddies. The material surfaces spin around the streamwise axes of these eddies, which are located at the streamwise boundaries and middle of the domain. This motion is accompanied by the thinning of the strip in the region separating neighbouring streamwise vortices, thus producing a 'hairpin' vortex configuration. The resulting deformation of the flow map is captured by the mesh refinement algorithm which can also be observed in the surface plots. Since the flow is inviscid,

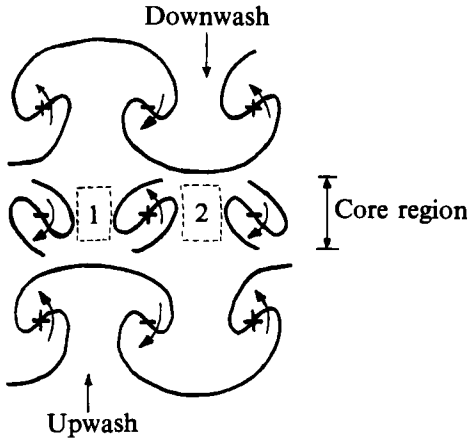

FIGURE 5. Schematic illustration of the evolution of the scalar distribution in the streamwise plane dividing the spanwise eddy core. The dashed rectangles show where the core leaves the plane of the figure: 1, outwards; 2, inwards.

the division and change of shape of the transport elements describes the strain field, especially when the elements approach the spanwise core or when they are attracted towards the axes of the vortex rods.

The adaptive response of the numerical scheme is illustrated in table 1 where the surface area, A, and of the number of elements, N, used along individual material surfaces are given. While both grow rapidly following the rollup of the vorticity layer, the increase in the number of transport elements occurs at a higher rate than that of the surface. Though the middle surface deforms at higher rate and carries a larger number of transport elements than the remaining surfaces, small zones of high strain exist along all material surfaces. These zones necessitate the introduction of new elements, an effect which precedes the severe deformation of the surfaces.

Figure 4 shows cross-sections through all the material (computational) surfaces at the time the computations are stopped, $t = 18.0$. (As indicated below, the structure of the flow field does not vary appreciably for $t \geqslant 16$ due to saturation of the instabilities. This additional frame is provided to emphasize this feature of the computed flow; the subsequent discussion will be limited to results obtained for $t \leqslant 16$). We take streamwise cross-sections through the braid and core in the planes located at $x = 2.0\,(d)$ and $x = 6.6\,(c)$, respectively, and spanwise sections along the planes $y = 1.6\,(b)$ and $y = 3.3\,(a)$. Small circles, whose radii are chosen smaller than the core radius, are drawn to mark the intersection points with the transport elements. The streamwise sections, (c) and (d), show how the streamwise rods, resulting from the rollup of the braids, give rise to the formation of the mushroom structures (Bernal & Roshko 1986; Lasheras *et al.* 1986; Lasheras & Choi 1988). They also depict how the extension of these rods around the spanwise cores results in the establishment of a double mushroom structure (Lasheras & Choi 1988). The results show that the deformation of the material surfaces within the core is due to the combined effect of three rows of streamwise vortex structures: two rows resulting from the extension of vortex rods towards the core, and a third generated by the deformation of the core itself under the action of the translative instability. This is shown schematically in figure 5.

The spanwise sections illustrate the effect of the translative instability on the cross-stream position of the core and the shape of its cross-section. Figure 4 shows

(a)

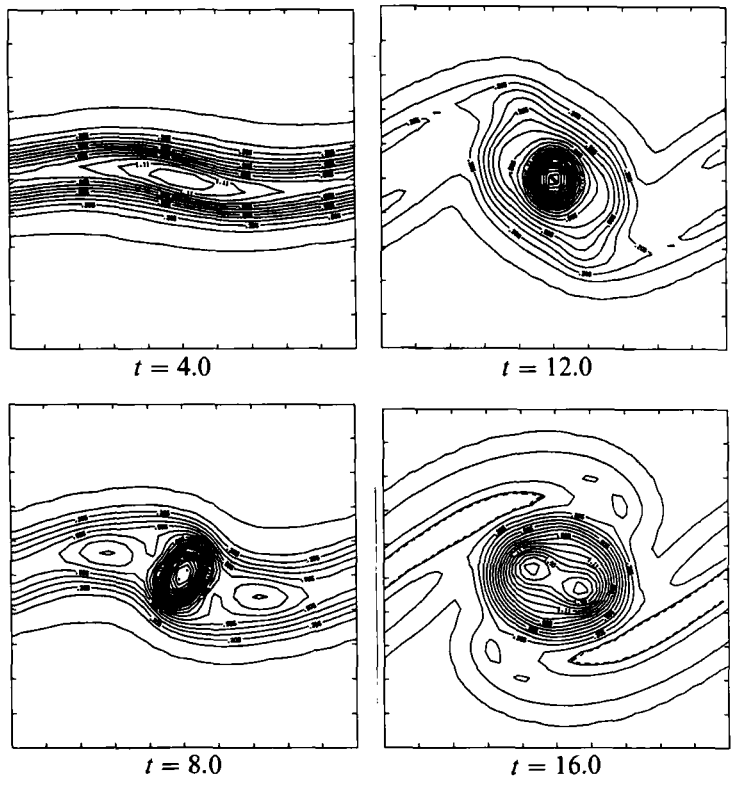

FIGURE 6(a). For caption see facing page.

that the core is pushed upwards and in the flow direction of the top stream in the 'left' half of the domain, $0 < y < \frac{1}{2}\lambda_y$, while it suffers an antisymmetric deformation in the other half, as can be seen in figures 2 and 3. The core loses its symmetry at most spanwise stations, as computational elements migrate in the direction opposite to that of the core translation. The distribution of material particles in the plane $y = 3.3$, which intersects the central streamwise vortex rod, shows that the braids significantly thicken at this critical spanwise location by entraining irrotational fluid from one side of the layer to the other. This is verified by simultaneously examining the streamwise cut through the plane $x = 6.6$, which illustrates the entrainment of the mushrooms around the spanwise core.

3.1.2. *Vorticity and scalar distributions*

The motion of the material surfaces follows the evolution of the vorticity field. This motion establishes entrainment patterns within the shear layer. Both are displayed in figures 6–9 in the form of vorticity and scalar contours plotted, respectively on two spanwise sections, $y = 3.3$ and 5.0, and on two streamwise sections, $x = 2.0$ and 6.6. The vorticity and scalar contours, generated using different techniques, are generated at times $t = 4.0$, 8.0, 12.0, and 16.0. Vorticity contours are generated by using the core smoothing functions to compute the vorticity on a mesh of 40×40 points and processing the data with the NCAR contouring software. A considerable amount of smoothing is introduced in this procedure, and the resulting plots are mainly used to deduce the large-scale features of the vorticity field. A

(*b*)

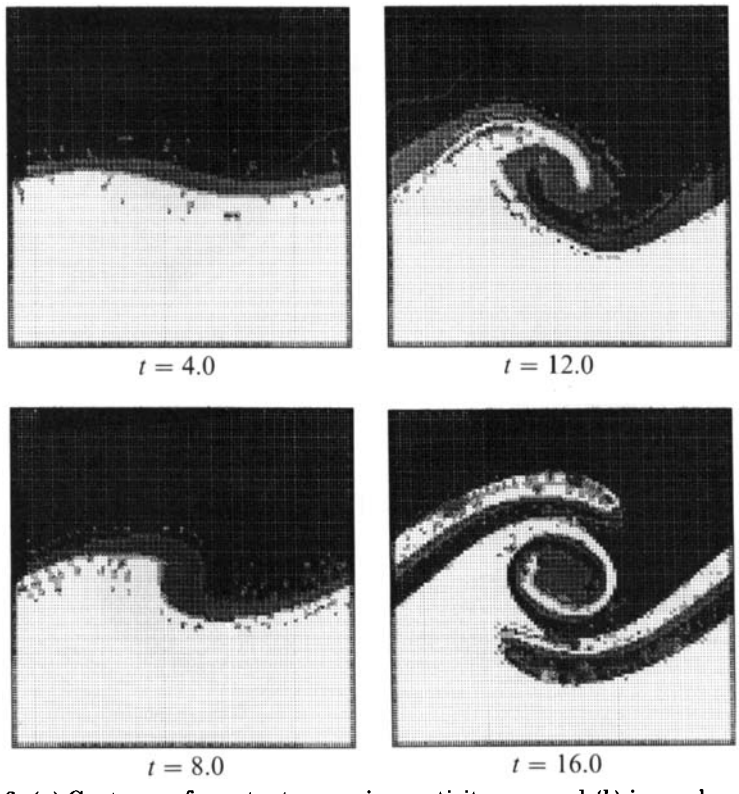

FIGURE 6. (*a*) Contours of constant spanwise vorticity, ω_y, and (*b*) iso-scalar contours plotted in the plane $y = 3.3$.

different approach, in which shaded areas of constant scalar concentration are generated by interpolating the discrete scalar values on a 135×135-cells grid, is adopted in the representation of scalar distribution.

(*a*) *Early stages of the three-dimensional motion*

At early stages, and until $t = 8.0$, the vorticity and scalar contours plotted at various spanwise sections are similar, indicating that the growth of the three-dimensional perturbations is suppressed during the early stages of the two-dimensional instability and that the spanwise vorticity remains essentially uniform across the layer (Metcalfe *et al.* 1987). Weak streamwise structures which change their form between different streamwise stations develop, but have not yet gained enough strength to alter the flow significantly. Meanwhile, a single row of counter-rotating vortices is found to repeat itself at all streamwise locations of the domain. These structures are generated by tilting of the vortex lines which, at $t = 0$, do not possess a streamwise vorticity component. The tilting of the vortex lines into the streamwise direction(s) leads to the creation of zones of alternating streamwise vorticity whose locations and signs follow the shape of sinewave perturbation. For $t > 4$, the streamwise vorticity is lowly intensified under the two-dimensional strain field, producing higher values in the braids of the eddy. With the rollup of the vorticity layer and the formation of a spanwise core, the edges of the core are stretched up and down towards the free streams, giving rise to the top and bottom rows of counter-rotating vortices which appear in figure 8(*a*). These two rows are

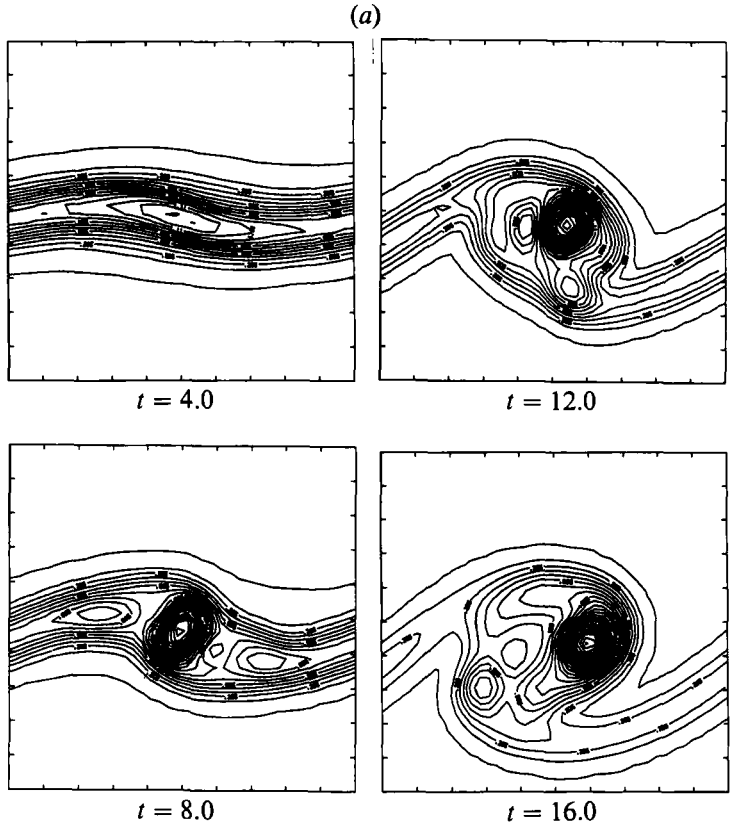

FIGURE 7(a). For caption see facing page.

separated by a third, which appears as a small circle whose vorticity is of the opposite sign to the previous two. As shown before, the latter is generated as a result of the growth of perturbations on the core itself by the translative instability mechanism.

(b) *Late stages of three-dimensional motion*

For $8.0 < t < 12.0$, the flow field suffers a rapid transition to three-dimensional motion leading to an intensification of the streamwise vorticity in the braids. The total circulation of the streamwise vortices, $\Gamma_{\text{tot}} = \int |\omega_x| \mathrm{d}A$ in the plane $x = 2.0$, increases from $\Gamma_{\text{tot}}(8) = 2.617$ to $\Gamma_{\text{tot}}(12) = 4.492$. The streamwise vorticity grows under the action of the strong strain exerted by the large spanwise cores in the neighbourhood of the stagnation 'lines' which anchor the braids (Lasheras & Choi 1988). Meanwhile, the deformation of the core, which is attributed to the growth of the translative instability, changes the alignment of the vorticity from predominantly spanwise into spanwise and streamwise components. Although the maximum value of streamwise vorticity occurs within the braids, the streamwise eddies generated by the core deformation have higher total circulation. At $t = 12.0$, the middle row of streamwise vortices in figure 8(a) accounts for 65% of the total circulation in the plane of the core. This is because the growth and maturation of the primary two-dimensional instability, which precede the three-dimensional motion, force the migration of the spanwise vorticity from the thinning braids into the core.

The total streamwise circulation in the plane dividing the core, $x = 6.6$, used as a measure of the three-dimensional effects in the flow, is shown in figure 10. It confirms

(*b*)

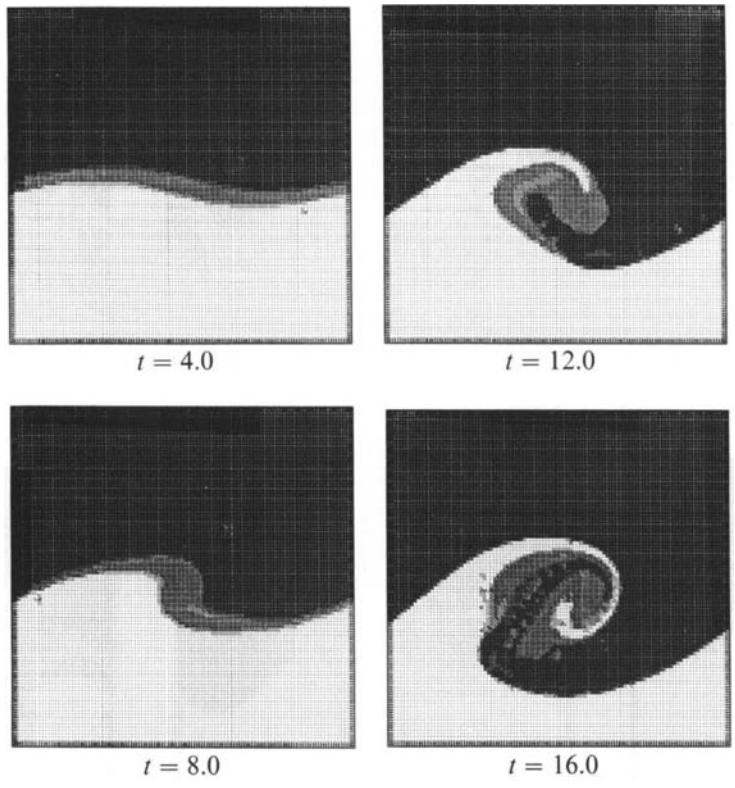

FIGURE 7. (*a*) Contours of constant spanwise vorticity, ω_y, and (*b*) iso-scalar contours plotted in the plane $y = 5.0$.

the early observation that three-dimensional effects are small during the linear stages of the two-dimensional instability and grow rapidly after rollup. The behaviour of the curve changes from an algebraic growth for $t < 9$, to an exponential growth between $9 < t < 13$. At later stages, a nonlinear regime characterized by a drop in the rate of increase of the total circulation is observed. This is expected since the strain field induced by the spanwise eddy leads to continuous intensification of the streamwise vorticity. For $t > 16.0$, no qualitative changes in the structure of the vorticity and scalar fields is observed, an indication that the instabilities tend to saturate (Metcalfe *et al.* 1987).

At late stages, the streamwise vortices induce a strong secondary motion. As previously indicated, this motion can be easily analysed in the braids of the eddy where scalar mushroom structures are generated. However, the scalar distribution is more complex in the core, where the flow is under the combined influence of spanwise and streamwise vortices. The top and bottom mushrooms, which forms due to the rollup of the braid vorticity and are identified in figure 8(*b*), originate in the braids and are then entrained towards the cores. Near the axis of the core, the scalar distribution is affected by the flow field induced by the three rows of alternating streamwise vortices shown schematically in figure 5. The superposition of the fields of these vortices, whose axes are deformed under the action of the translative instability, leads to the generation of 'W-shaped' scalar structures.

The spanwise vorticity contours at $t = 12.0$, although similar to those encountered in a two-dimensional flow, exhibit a more compact core than in two dimensions due

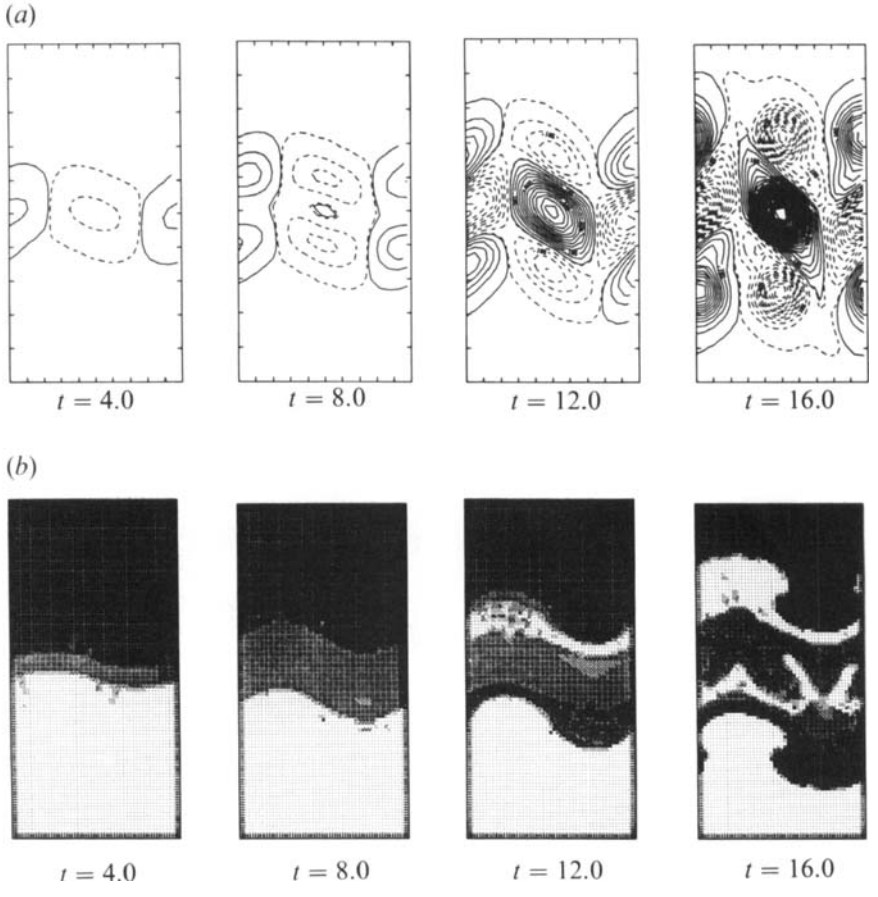

FIGURE 8. (a) Contours of constant streamwise vorticity, ω_x, and (b) iso-scalar contours plotted in the plane $x = 6.6$.

to stretching along the axis of the core. The stretching of spanwise vorticity is accompanied by a non-uniform deformation of the cores at different spanwise locations. The corresponding variation of the spanwise vorticity is depicted in the last frames of figures 6 and 7. The core is shifted towards and in the direction of the bottom stream for $\frac{1}{2}\lambda_y < y < \lambda_y$, while it suffers an antisymmetric displacement for $0 < y < \frac{1}{2}\lambda_y$ (see also figures 2 and 3). This confirms the results of the linear stability theory of perturbed vortex cores which predicts a 'translative' instability of the cores in the manner described above (Pierrehumbert & Widnall 1982). We also note that the point of maximum vorticity within the core, which moves in the direction opposite to that of the outer boundaries of the core, no longer coincides with its geometric centre. This configuration resembles that observed in the evolution of the eigenfunctions of the linear stability problem of vortex rings, which also predicts a similar behaviour for any locally curved vortex filament (Widnall & Tsai 1977). We recall that the most amplified mode of the translative instability mechanism is characterized by an eigenfunction which changes sign within the vorticity core. This property also arises in the linear stability of vortex rings as a necessary condition for eigenfunction instability. In both cases, the amplification of the instability forces the migration of the 'inner' core in the direction opposite to the motion of its outer boundaries.

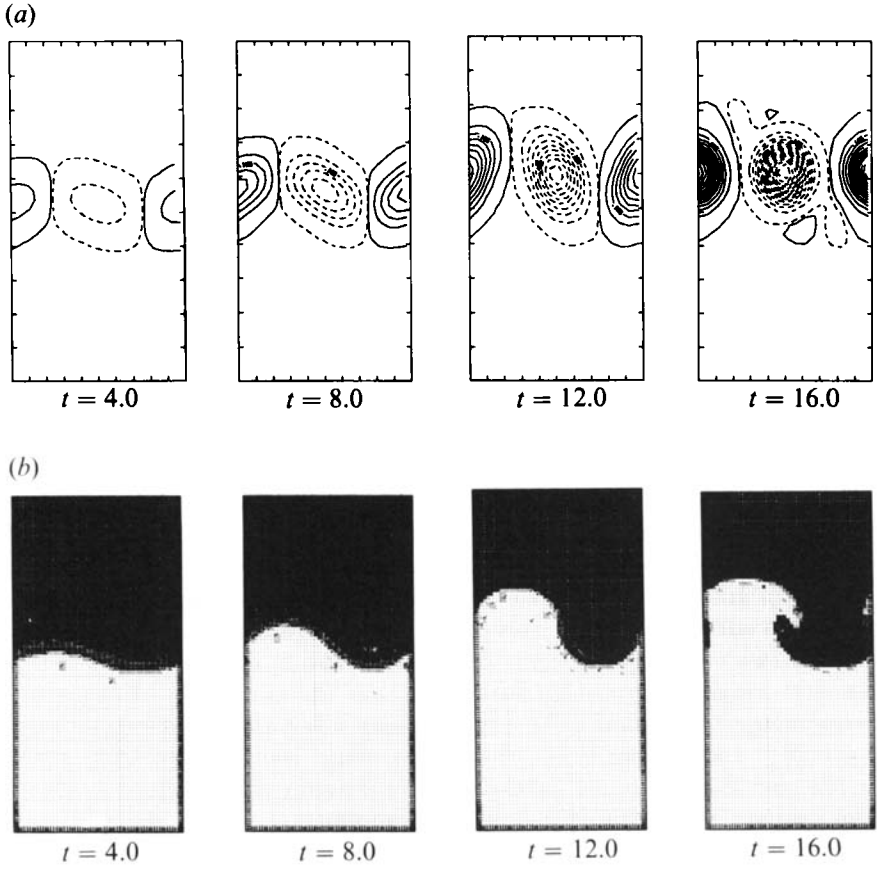

FIGURE 9. (*a*) Contours of constant streamwise vorticity, ω_x, and (*b*) iso-scalar contours plotted in the plane $x = 2.0$.

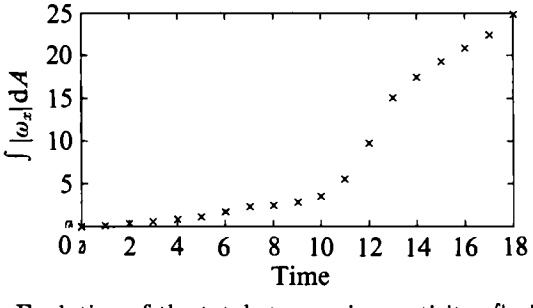

FIGURE 10. Evolution of the total streamwise vorticity, $\int|\omega_x|\mathrm{d}A$, computed in the streamwise plane located at $x = 6.6$.

This mechanism appears to be connected to convective currents within the core and not to uneven vorticity stretching. This is verified by inspecting the scalar distribution in the same cross-sections, which shows that the scalar field follows a similar redistribution and loses its symmetry. This motion leads to preferential entrainment of irrotational fluid from the free streams. The section of the core which is displaced upwards, $0 < y < \frac{1}{2}\lambda_y$, entrains more fluid from the bottom stream, while the section which is pushed downwards consists mainly of the top-stream fluid. This

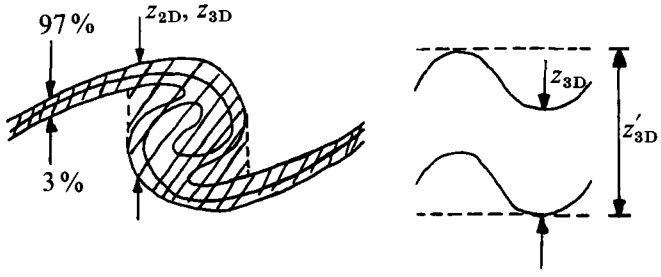

FIGURE 11. Schematic illustration of the eddy.

form of preferential entrainment resembles that reported experimentally (Bernal & Roshko 1986).

The symmetry of the vorticity and scalar distributions is preserved at the spanwise mid-section of the domain, since, as predicted by the theory, the curvature of the core vanishes at that location. Nevertheless, this plane is of interest since it intersects the streamwise vortex rod centred in the domain (see figures 2 and 3). This rod appears in the form of a 'tongue' of negative vorticity which extends through the braids to the top and bottom edges of neighbouring cores (figures 6*a*, $t - 16.0$). At this plane of zero curvature, the action of the translative instability is manifested by the presence of two vorticity maxima. A similar vorticity distribution is obtained in unstable vortex rings at azimuthal stations where the curvature of the axis of the core vanishes (Knio & Ghoniem 1988). In the shear layer, these stations lie within the planes $y = 0, \frac{1}{2}\lambda_y$, and λ_y, while, in the vortex ring, the local curvature vanishes whenever the curvature induced by the growth of azimuthal bending waves cancels that of the undisturbed vortex ring. The resemblance between the two cases has important implications for the implementation of numerical schemes and the modelling of the vorticity layer. The numerical study in Knio & Ghoniem (1990) shows that the dynamics within concentrated vortices may not be properly predicted unless a sufficiently large number of computational elements is used to discretize the vortex cores. As a result, the computations could have missed or spuriously predicted the evolution of the translative instability, had we chosen to simulate the vorticity layer by distributing the transport elements on a single material layer, or to model the layer as a thin vortex sheet, as in Ashurst & Meiburg (1988) and Inoue (1989).

3.1.3. *Entrainment enhancement*

The development of the three-dimensional instabilities promotes shear-layer entrainment (Knio & Ghoniem 1991). To quantify this effect, the shear layer entrainment is measured by introducing an 'eddy size' parameter, S, in two and three dimensions. In two dimensions, the eddy size is defined by measuring the region enclosed between the surfaces where the normalized scalar first deviates b 3% from the corresponding free-stream value. This yields a local height of the eddy, $Z_{2D}(x)$, which, when integrated over the streamwise length of the domain, gives a mean eddy size,

$$S_{2D} = \int_0^{\lambda_x} Z_{2D}(x)\,\mathrm{d}x. \tag{10}$$

According to this definition, the eddy consists of the union of the rotational fluid and the irrotational fluid trapped between the braids and the core (see figure 11). In three dimensions, two similar definitions are considered. The first is obtained by measuring

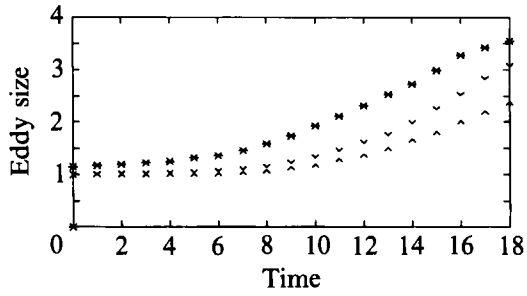

FIGURE 12. Evolution of the eddy size of two dimension, S_{2D} (∨), and in three dimensions, S_{3D} (∧), and S'_{3D} (*).

the height of the eddy at each spanwise and streamwise location, $Z_{3D}(x, y)$, and then integrating over the spanwise and streamwise periodicity length to get an eddy size,

$$S_{3D} = \int_0^{\lambda_x} \int_0^{\lambda_y} Z_{3D}(x, y)\, dy\, dx. \tag{11}$$

While this definition is a natural extension of that in two dimensions, the contribution of the irrotational fluid trapped by the mushroom structures is neglected in the averaging process. To account for this additional entrainment mechanism, we define a third measure, S'_{3D}, by

$$S'_{3D} = \lambda_y \int_0^{\lambda_x} Z'_{3D}(x)\, dx, \tag{12}$$

where $Z'_{3D}(x) = \max_y (Z_{3D}(x, y))$.

The eddy size is normalized by the spanwise and streamwise periodicity lengths in three-dimensional computations and by the streamwise periodicity length in two dimensions, so that the resulting values represent an average thickness of the scalar distribution. The entrainment enhancement is shown in figure 12 by comparing the eddy size for two- and three-dimensional computations. With the rollup of the layer, $t \sim 8.0$, entrainment curves start to grow with the curves in three dimensions acquiring a higher growth rate. The deviation in the behaviour of the two- and 3-dimensional solutions coincides with the three dimensional transition depicted in figure 11. Thus, the transition to three-dimensional motion is accompanied by an 'entrainment transition'. By the end of the simulation, the total entrainment S'_{3D} increases by 75 % over its two-dimensional counterpart, while comparison of S'_{3D} and S_{3D} indicates that the formation of the mushroom structures contributes significantly to entrainment enhancement.

The eddy size parameters are also used to quantify the preferential entrainment of fluid at various sections of the domain. This form of entrainment reverses itself every half spanwise wavelength so that the composition of the eddy does not favour either free stream. However, in the region $0 < y < \frac{1}{2}\lambda_y$, preferential entrainment of lower-stream fluid is observed. Preferential entrainment may be estimated by subdividing the integrals in (10)–(12) over the regions defined by: $s > s_{a\nu}$, and $s < s_{a\nu}$, thus yielding: $(S_{3D})^+$, $(S_{3D})^-$, $(S'_{3D})^+$, and $(S'_{3D})^-$. At $t = 16.0$, the entrainment ratios in the area $0 < y < \frac{1}{2}\lambda_y$, $(S_{3D})^-/(S_{3D})^+ = 1.787$, and $(S'_{3D})^-/(S'_{3D})^+ = 3.487$. These ratios are reversed in the area $\frac{1}{2}\lambda_y < y < \lambda_y$, so that unit net entrainment ratios are obtained. The difference between the two ratios is a manifestation of the role of streamwise vortices in inducing preferential entrainment patterns (Bernal & Roshko 1986).

3.1.4. *Discussion*

The results of the computations show that the evolution of the shear layer from a perturbed steady state using monochromatic three-dimensional disturbances consists of three stages. (i) In the first stage, an essentially two-dimensional growth of the perturbations, in the form of linear amplification of the Kelvin–Helmholtz instability modes, is observed. During this phase, all three-dimensional activity is suppressed. This is followed by a nonlinear two-dimensional growth of the fundamental mode, leading to rollup and the formation of a concentrated spanwise eddy core. (ii) The rollup is accompanied by a rapid growth of the three-dimensional modes, in the form of a deformation of the spanwise eddy and an instability in the braids. (iii) The three-dimensional modes undergo a nonlinear growth which results in the redistribution of the streamwise vorticity into vortex rods and in the generation of the scalar mushroom structures.

While the two-dimensional instability is relatively simple to describe, the three-dimensional motion in the cores and braids of the vortex structures are more involved. The stability of the rolled layer was examined by Pierrehumbert & Widnall (1982) using a periodic array of Stuart vortices. They found that this array was linearly unstable to a mode they called the translative instability, which leads to a deformation of the spanwise eddies according to the strain field induced by the eddy and by its image vortices. The instability appearing in the braids was studied in the work of Corcos & Lin (1984), who proved the fundamental nature of the instability of a strained streamwise vorticity and showed that the growth of this mode is suppressed during the amplification of the two-dimensional instability. The translative instability is fundamentally different from the Corcos mechanism since the braids of the spanwise vortices, observed in the case of a shear layer, are not well represented by the Stuart vortices. Thus, the two instabilities differ in form. The translative mode is an instability of the spanwise cores, that is of large concentrated vortices subject to strain normal to their axes, while the Corcos mechanism predicts the instability of streamwise vorticity when subjected to strong extensional strain.

The absence of braids does not preclude the formation of vortex rods by the strain field which may cause the vorticity within the core to migrate outwards preferentially (Grinstein *et al.* 1989). On the other hand, the ability of the streamwise vortex rods generated by the Corcos mechanism to impart a core deformation similar in shape to that obtained by the development of the translative instability (Corcos & Lin 1984) complicates the task of separating the role of these two instabilities. This difficulty has led researchers (Ashurst & Meiburg 1988; Lasheras & Choi 1988) to emphasize the importance of a nonlinear interaction between the spanwise cores and the streamwise vortices. Our results, however, indicate that the translative instability within the cores grows simultaneously with the intensification of the rods. Since, as previously mentioned, a mild straining of the streamwise vorticity is observed prior to the rollup of the spanwise vorticity, and since the translative instability is a linear instability mechanism, the importance of such an interaction should be played down.

The formation of the streamwise vortex rods leaves its mark on the flow in the form of scalar mushroom structures. The translative instability, on the other hand, is manifested by an asymmetric spanwise vorticity distribution within the core, which resembles that predicted by the growth of unstable eigenfunctions of the Widnall instability of vortex rings (Widnall & Tsai 1977). The alternating preferential entrainment patterns which result from the amplification of the instability mode compound the difficulty in experimentally visualizing the scalar structures

mentioned by Corcos & Lin (1984), since uniform-density spatially developing shear layers entrain more fluid from the faster stream (Dimotakis 1986). Despite these difficulties, a deformation consistent with the development of the translative instability was inferred by Jiminez (1983) and by Bernal & Roshko (1986) based on spanwise correlations of velocity fluctuations.

The analysis of the evolving vorticity structures using numerical simulation makes a valuable contribution since direct and detailed measurements of the vorticity field are usually not possible or extremely cumbersome. Such difficulties are primarily encountered in experimental studies in which velocity correlations (Browand & Troutt 1980; Jiminez 1983; Wygnansky *et al.* 1979), passive scalar or dye techniques (Bernal & Roshko 1986; Jiminez *et al.* 1985), or low-heat-release chemical reactions (Breidenthal 1981; Lasheras *et al.* 1986; Lasheras & Choi 1988) have been used as substitute tools for deducing the topology of the vorticity field. Our results suggest that such efforts should be conducted with great care, because a large number of mechanisms contributes to their formation. The computed results reveal some of the difficulties arising from the lack of an accurate knowledge of the vorticity field. In particular, it is shown that the deformation of material surfaces, visualized for instance by injecting marker particles in one of the fluid streams, may not be sufficient to fully determine the corresponding vortical structures, especially if one cannot *a priori* locate a given material surface with respect to the layer of highest spanwise vorticity. The rapid variation of the strain field around the latter causes substantially different deformations of adjacent layers, thus preventing immediate correlations with the underlying vortical structures. On the other hand, the visualization of vorticity structures by means of the products of a unity-stoichiometry, low-heat-release chemical reaction may remove some of these difficulties, since, as observed by Knio & Choniem (1992), the products of reaction are always entrained into zones of high vorticity.

3.2. *Variable-density shear layer*

Density variation, characterized by a density ratio of the free streams, plays an important role in the evolution of heterogeneous shear layers created by the merging two streams of unequal density and velocity. It has been observed that a non-unity density ratio alters the spatial growth of the layer and influences the entrainment induced by the vortical structures embedded therein, even when gravity effects are weak (Brown & Roshko 1974; Ho & Huerre 1984; Dimotakis 1989). In chemically reacting flows, density variation is generated by heat release which leads to the generation of zones of high temperature and low density. Here too, the presence of two or more zones of different density is found to affect the stability and development of the flow. This effect depends on both the details of the density and vorticity distributions, as it may constitute a stabilizing or a destablizing mechanism (Riley & McMurtry 1989; McMurtry, Riley & Metcalfe 1989; Ghoniem & Krishnan 1988).

In this section, the effect of weak density variation on three-dimensional instability is investigated by computing the onset of three-dimensional motion in an incompressible, variable-density shear layer. While this study is ultimately motivated by the desire to predict high-heat-release reactions in vortical flows, the simplified model allows us to focus on the dynamic effects of baroclinic vorticity. In a three-dimensional flow, this stepwise approach is important because of the presence of a vorticity stretching term. One case with small density ratio, $\rho_{max}/\rho_{min} = 2$, is considered. To avoid a re-initialization of the scalar (density) gradient field, we use

the same discrete scalar gradient values as the previous case but set $\rho_{av} = 1.5$. Therefore, in a high-density top free stream, $\rho_{max} = 2$, and in the low-density bottom free stream, $\rho_{min} = 1$. The same initial perturbation used in the previous case is applied, and the computations are performed to observe the growth of both the two- and three-dimensional instabilities.

The linear theory of variable-density shear layers (Ghoniem & Krishnan 1989; Krishnan 1989) shows that the wavelength of the most amplified mode of the two-dimensional instability depends weakly on, and the growth rate are almost independent of, the density ratio, while its phase velocity varies strongly with the density ratio. Unlike the uniform-density case, the most amplified mode in the variable-density layer evolves as a travelling wave moving in the direction of the high-density stream with phase speed increasing with the density ratio. This effect has been used to explain the difference in growth rates in variable-density, spatially evolving layers (Dimotakis 1989, 1986; Brown & Roshko 1974; Ghoniem & Krishnan 1989). For the density and vorticity profiles used in the simulation, and a density ratio of 2, the linear stability theory predicts a phase speed $c = 0.17$. We note that the stability analysis performed by Ghoniem & Krishnan (1989) differs slightly from the earlier investigation of Maslowe & Kelly (1971), who showed that, in the limit of vanishing Richardson number, density stratification tends to stabilize a temporal shear layer. The differing conclusions are due to the assumed density profiles. The analysis of Maslowe & Kelly, which was primarily concerned with atmospheric and oceanic flows, assumed an exponentially varying density distribution. This distribution is contrasted with the error-function profile which is more representative of high-speed shear flows, where small Richardson numbers are more frequently encountered.

The effect of the density variation on the linear stability of three-dimensional perturbations is not known at present. Three-dimensional instability of variable-density shear layers is not a simple extension of that of the uniform-density case since one must deal with the added difficulty of formulating a steady initial condition of the stability problem. In the uniform-density case, Stuart vortices were used to approximate the flow of the rolled layer (Pierrehumbert & Widnall 1982). The existence of similar solutions in the variable-density case is complicated by the convective motion of the vortices due to the baroclinic generation of vorticity, as observed in two-dimensional simulations (Ghoniem & Krishnan 1989). As a result, and because we have approached the study of three-dimensional temporal layers with the intention of investigating deviations from the two-dimensional case, we were content with keeping the same spanwise periodicity length used in the uniform-density case. This prompted us to select a small value of the density ratio, so that comparisons with the preceding results are justified.

3.2.1. *Deformation of material surfaces*

Figure 13 shows the evolution of a material surface initially lying in the planes $z = 0$. At early stages, the motion of the middle layer bears strong resemblance to its counterpart in the uniform-density case (figure 2). This similarity is expected, and in agreement with the results of the linear stability theory which predicts almost identical growth rates of the two-dimensional perturbation. The first manifestation of the convective motion of the instability wave is observed once the rollup of the layer is completed and a well-defined eddy core is formed ($t > 8$). During this period, the three-dimensional perturbation is amplified causing the core to deform in the way similar to that predicted by the translative instability of uniform-density cores.

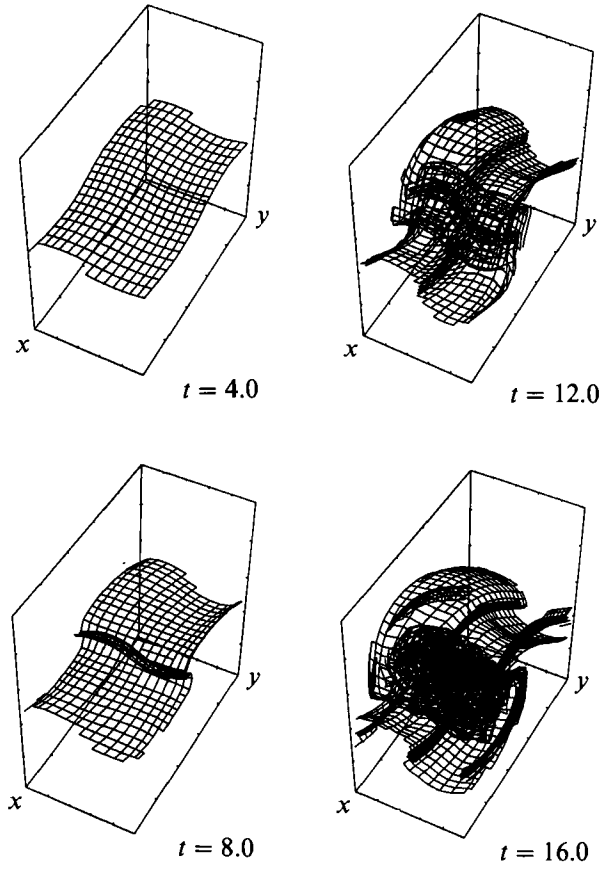

FIGURE 13. Three-dimensional perspective view of the surface $\rho' = 0$, initially lying in the plane $z = 0$ for the case of a variable-density shear layer. The plots were generated from the point of view of an observer located at (48, 24, 48).

Material layer	z location	$t = 4.0$		$t = 8.0$		$t = 12.0$		$t = 16.0$	
		A	N	A	N	A	N	A	N
1	−1.32	1.03	1.00	1.12	1.30	1.70	2.00	3.47	4.75
2	−0.66	1.04	1.00	1.22	1.40	2.35	2.84	4.74	7.75
3	0	1.04	1.00	1.43	1.55	2.71	3.65	5.48	10.11
4	0.66	1.04	1.00	1.21	1.41	2.22	2.93	4.78	8.63
5	1.32	1.03	1.00	1.12	1.28	1.57	1.71	3.11	3.80

TABLE 2. Normalized surface area, A, and number of elements, N, for the individual material layers

However, the (deformed) axis of the core no longer coincides with the streamwise mid-section of the domain, but shifts in the positive streamwise x-direction, i.e. in the direction of the high-density top stream. The braids suffer a deformation whose shape is of the same type as observed in the uniform-density case.

The total surface area of the material surfaces and the number of transport elements, shown in table 2, exhibit the same trends as described in the uniform-density case. However, the motions of surfaces lying on the top and bottom sides of the middle layer are no longer similar because of the asymmetry of the flow field.

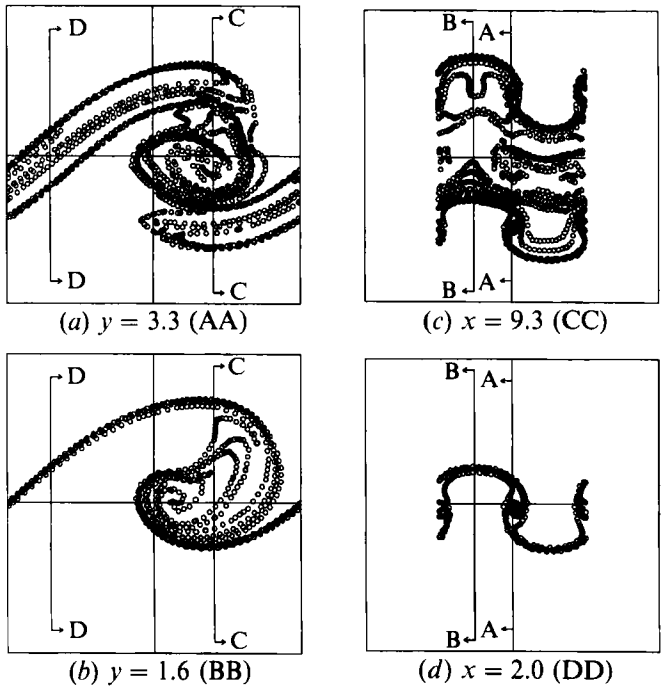

FIGURE 14. Intersection of the Lagrangian mesh at $t = 16.0$ with the planes (*a*) $y = 3.3$, (*b*) $y = 1,6$, (*c*) $x = 9.3$, and (*d*) $x = 2.0$.

Prior to the maturation of the three-dimensional instability, $t < 12.0$, the material surfaces lying on the low-density side are deformed at higher rate than those located in the heavier fluid side of the layer. At later stages, this trend is reversed. This asymmetric straining of the surfaces is related to the asymmetry of the spanwise vortices whose rotation resembles the eccentric spinning of egg-shaped cores.

While the uneven deformation of the braids is readily verified at later stages, the asymmetric stretching of streamwise vorticity affects the entrainment patterns in the neighbourhood of the spanwise cores (Brown & Roshko 1974; Dimotakis 1986, 1989; Ghoniem & Krishnan 1989). However, the motion of the Lagrangian mesh cannot be used to deduce this effect because the vorticity lines in a variable-density flow cannot be directly identified with material lines, and the deformation of material surfaces is not sufficient to completely determine the fate of the vorticity. In fact, detailed examination of the motion of the material surfaces only indicates that, in the braids, streamwise vorticity reorganizes into rods, leading to the formation of the mushroom structures that cover the eddy cores, and that the spanwise cores propagate in an asymmetric flow field.

Signs of the influence of the baroclinic vorticity and the associated asymmetry of the strain field on the evolution of the three-dimensional perturbation appear in the cross-sections through the material surfaces. These sections, shown at $t = 16.0$ in figure 14, are generated on a streamwise section translated in the direction of the heavy stream to $x = 9.3$ in order account for the convective motion of the eddy. The mean streamwise location of the core is first estimated by translating the plane $x_{\frac{1}{2}} = 6.6$ by ct, c being the phase speed of the two-dimensional Kelvin–Helmholtz wave obtained from the linear theory. This estimate is then refined by considering the neighbouring planes on both sides of the plane $x = x_{\frac{1}{2}} + ct$. It is found that the mean

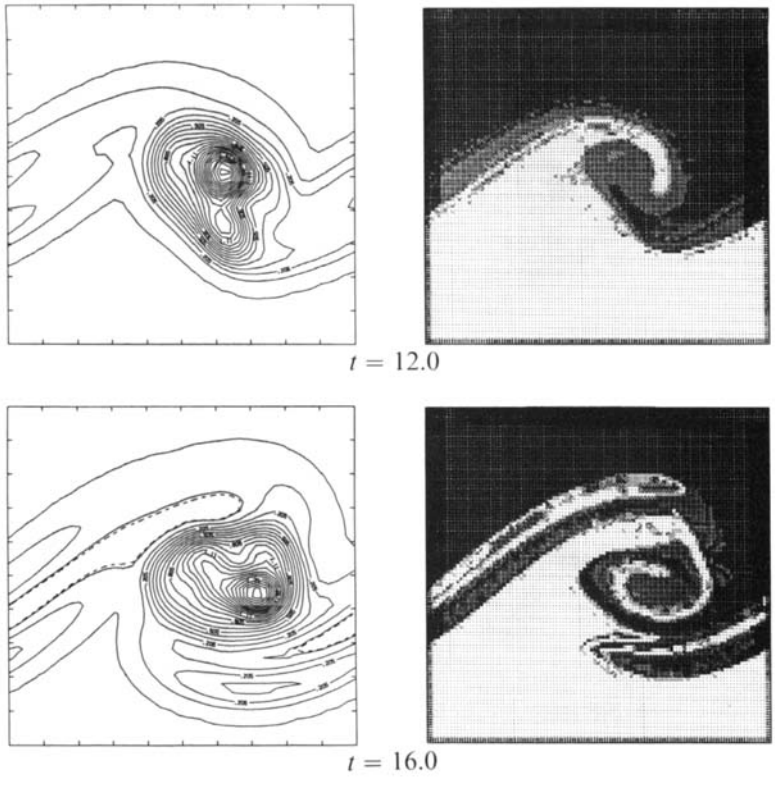

FIGURE 15. Contours of spanwise vorticity, ω_y, (left) and density (right) plotted in the plane $y = 3.3$.

streamwise location of the eddy shifts from $x = 6.6$ at $t = 0$, to $x = 7.3$, 8.0, 8.6, and 9.3 at $t = 4.0$, 8.0, 12.0, and 16.0 respectively. Thus, the convective speed of the eddy is closely approximated by c even in the nonlinear stages (Ghoniem & Krishnan 1989). For the remaining sections, we still use the planes $y = 3.3$ and 1.6 to visualize the variations along the span of the layer, and the plane $x = 2.0$ to obtain a representative streamwise section of the braids.

The large-scale features of the instability in the variable-density flow can be approximated by those found in the previous case simply by accounting for the convective motion of the eddy. However, cross-sections through the core reveal that the mushrooms entrained on the top and bottom of the core are not similar. The top mushroom, lying on the side of the high-density fluid, is larger, more rounded, and less developed that its counterpart on the bottom side of the eddy. The concentration of computational elements, visualized by darker areas on the plots, is higher in the lower mushroom especially near the axes of the streamwise vortex rods. Thus, streamwise vorticity is higher for the bottom vortex rods, leading us to expect higher rates of spinning around their axes, and a significant departure from the entrainment patterns observed in the previous case.

3.2.2. *Vorticity and density fields*

The spanwise structure of the layer is shown in terms of the spanwise vorticity and density contours, plotted in figures 15 and 16 in the spanwise planes $y = 3.3$ and 5.0, respectively. The streamwise structure of the layer is examined by considering cross-sections through the core and the braid. The core cross-sections, figure 17, are

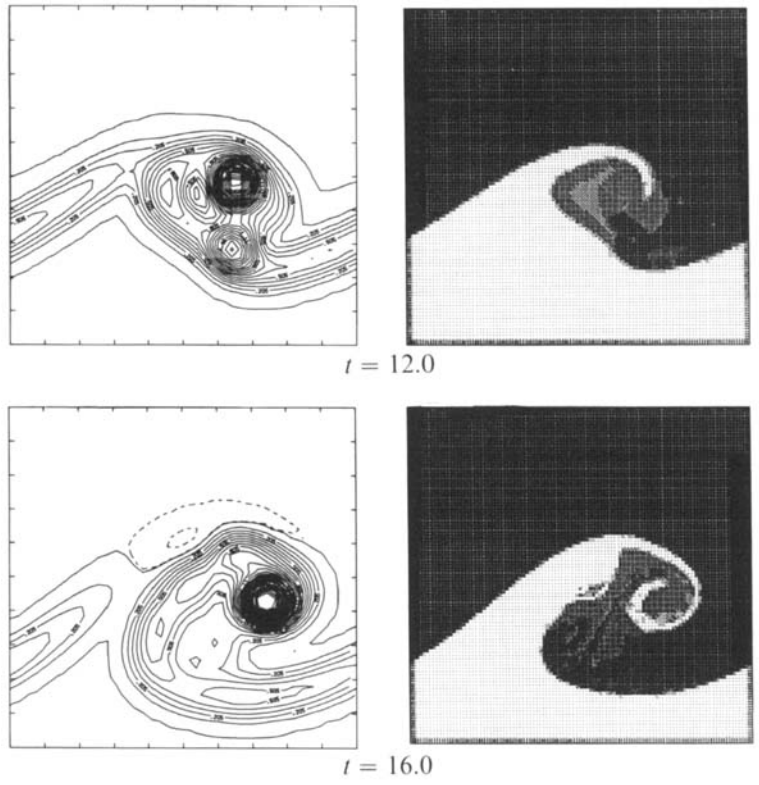

FIGURE 16. Contours of spanwise vorticity, ω_y (left) and density (right) plotted in the plane $y = 5.0$.

generated in the (y,z)-planes coinciding with the mean streamwise location of the eddy. We use the fixed streamwise plane $x = 2.0$ to cut through the braids, the results being shown in figure 18, at $t = 12.0$ and 16.0, i.e. following the growth of the three-dimensional modes.

A qualitative similarity between the uniform- and variable-density flow in terms of the types and shapes of vortical structures that are formed as a result of the evolution of the various instabilities is noticeable. The variable-density layer can be characterized by the same stages of evolution as the uniform-density layer: (i) an early growth of the Kelvin–Helmholtz instability during which the layer remains essentially two-dimensional; (ii) a nonlinear evolution accompanied by the formation of a spanwise core as a coherent eddy, the onset of the three-dimensional undulation along its axis, and the generation of streamwise vorticity; and (iii) a maturation of the translative instability, the redistribution of the streamwise vorticity into vortex rods, and the formation of scalar mushroom structures. The differences between the two cases, which arise owing to the baroclinic generation of vorticity, are summarized in the following.

(i) The evolution of the Kelvin–Helmholtz mode is modified by a finite phase speed of the waves in the direction of the high-density stream. The motion of the waves is uniform in all spanwise stations, and persists into the nonlinear stages.

(ii) The vorticity field loses its symmetry as a result of the vorticity generated by the baroclinic torque. The loss of symmetry is not restricted to any particular spanwise plane, and is not due to the amplification of three-dimensional modes as it is also observed in two-dimensional simulations Ghoniem & Krishnan 1989).

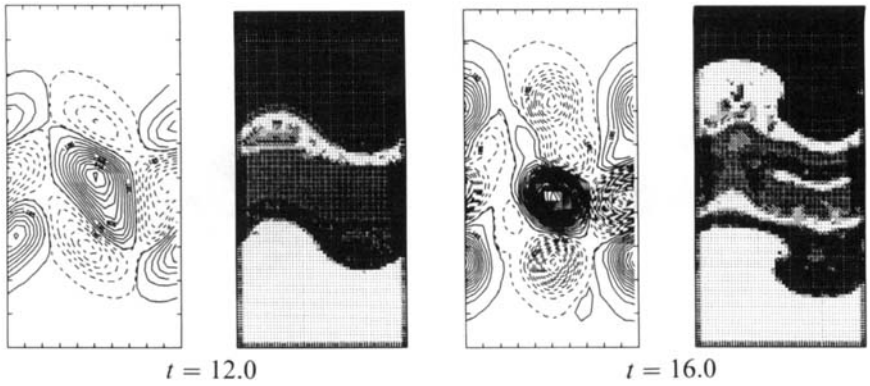

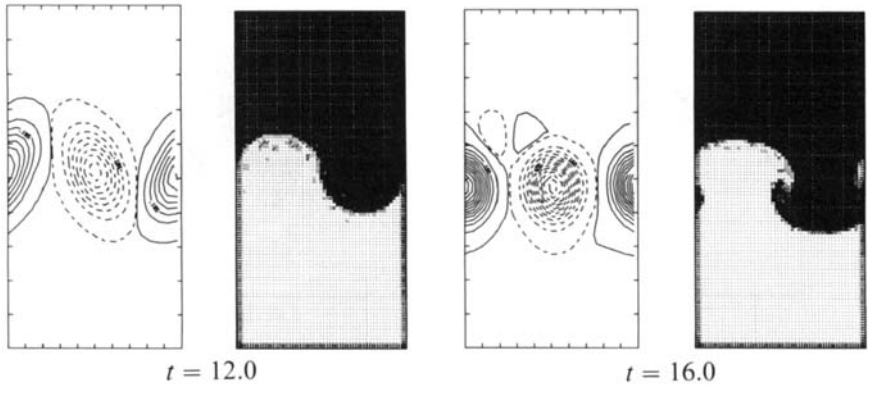

FIGURE 17. FIGURE 18.

FIGURE 17. Contours of streamwise vorticity, ω_x (left) and density (right) plotted at $t = 12.0$, and 16.0, in the planes $x = 8.6$, and $x = 9.3$ respectively.

FIGURE 18. Contours of streamwise vorticity, ω_x (left) and density (right) plotted in the plane $x = 2.0$.

(iii) The loss of symmetry affects the streamwise vorticity via its asymmetric strain field. For $t < 12.0$, the top layer of streamwise vortices, lying on the side of the high-density stream, is considerably weaker than its counterpart on the bottom side, while the trend is reversed at later stages. At $t = 12.0$, $\Gamma_{\text{top}}/\Gamma_{\text{bot}} = 0.536$, and increases to $\Gamma_{\text{top}}/\Gamma_{\text{bot}} = 1.12$ at $t = 16.0$. Thus, the strength of the streamwise vortices changes on both sides of the eddy in accordance with the deformation of material surfaces. This implies that, for $12.0 < t < 16.0$, the asymmetric straining of streamwise vorticity leads to the establishment of spanwise entrainment patterns which are biased towards the high-density side. This bias is due to the difference in strength of the streamwise rods wrapped on opposite sides of the spanwise core, and opposes the effect of the streamwise two-dimensional entrainment currents which favour low-density fluid.

(iv) The loss of symmetry is accompanied by a net asymmetric entrainment of the low-density fluid. We distinguish between the preferential entrainment associated with the growth of three-dimensional modes, and the entrainment asymmetry due to the baroclinic generation of vorticity. The asymmetric entrainment of the low-density fluid combines with the preferential entrainment of low-density fluid in

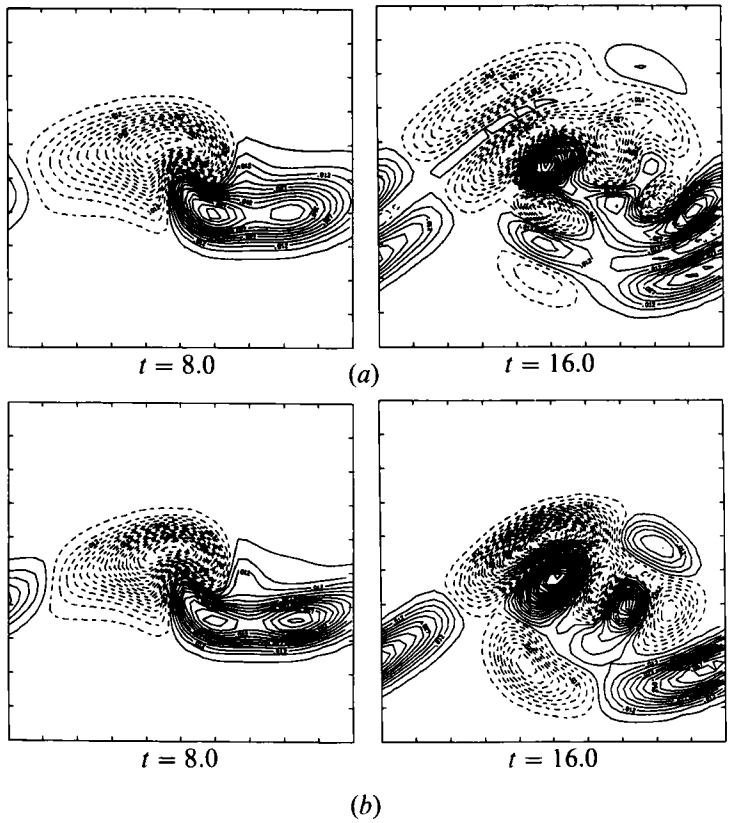

FIGURE 19. Contours of the spanwise component of the baroclinic torque, τ_y, plotted in the plane (*a*) $y = 3.3$ and (*b*) $y = 5.0$.

$0 < y < \frac{1}{2}\lambda_y$, produces an asymmetric distribution at the spanwise mid-section of the domain, and counteracts the effect of the three-dimensional instabilities in $\frac{1}{2}\lambda_y < y < \lambda_y$. At $t = 16.0$, the entrainment ratios, $(S_{3D})^-/(S_{3D})^+ = 2.541$, and $(S'_{3D})^-/(S'_{3D})^+ = 4.458$ in the area $0 < y < \frac{1}{2}\lambda_y$, while the net entrainment ratios, $(S_{3D})^-/S_{3D})^+ = 1.245$, and $(S'_{3D})^-/(S'_{3D})^+ = 1.140$. Thus, the spanwise entrainment patterns induced by the streamwise vortex rods lead to a reduction of the asymmetry in the entrainment ratio.

3.2.3. *Baroclinic vorticity*

In order to isolate the effects of the density variation from those associated with vortex stretching, the distribution of the baroclinic torque is used. Figure 19 shows the spanwise component of the baroclinic torque, τ_y, in the planes $y = 3.3$ and 5.0, while the streamwise component τ_x, is shown in figure 20 for the core and braid sections. At early stages, $t < 8.0$, the spanwise component of the baroclinic torque is concentrated in two zones of opposite sign. The initial vorticity of the layer is depleted in the left-hand side of the domain and enhanced in the remaining part. Thus, baroclinic vorticity imparts an asymmetry to the vorticity distribution such that the part of the layer displaced towards the high-density fluid is weakened, while that pushed in the direction of the low-density stream is intensified. As suggested in Ghoniem & Krishnan (1989), this asymmetry may be used to explain the origin of the motion of the Kelvin–Helmholtz mode.

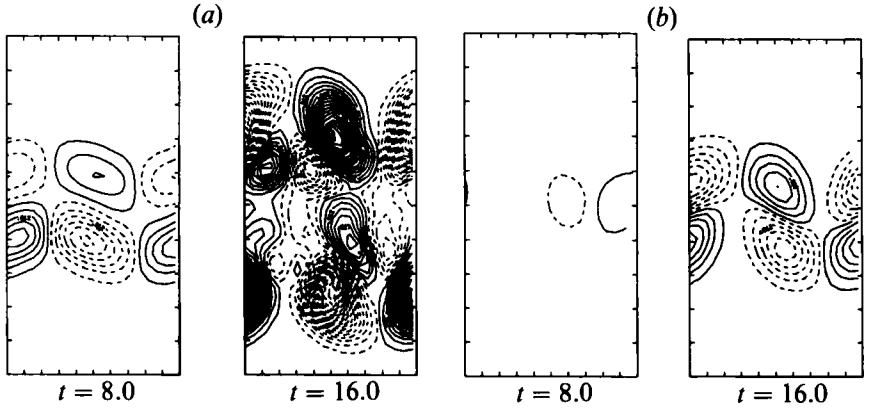

FIGURE 20. Contours of the streamwise component of the baroclinic torque, τ_x, plotted at $t = 8.0$ and 16.0, in (y, z)-planes given by (*a*) $x = 8.0$ and 9.3; and (*b*) $x = 2.0$.

Reduction of spanwise vorticity on the high-density side of the layer, and its enhancement on the low-density side is responsible for the observed difference in the strength of the streamwise vortices between the top and bottom rows of the core. As shown in figure 20, the streamwise component of the baroclinic term is extremely weak during the linear stages of the primary instability. Therefore, the asymmetry in the streamwise vorticity distribution must be due to the uneven tilting and stretching of layers of varying strengths so that density variation effects are primarily felt through changes in the spanwise vorticity.

At later stages, however, baroclinic torques becomes strong enough to directly affect the evolution of the streamwise vorticity. Density variation does not lead to a net intensification or weakening of the streamwise vortices in the braids since the baroclinic term changes sign within each streamwise eddy. Nevertheless, the baroclinic term is distributed in such a way as to weaken the top parts of the streamwise eddies and to strengthen their bottom parts, leading to a downward drift of the vortex rods. On the other hand, in the core, baroclinic torques contribute to the asymmetry between the top and bottom rows of streamwise vortices. While the middle row of vortices is affected in a similar way as that observed in the braids, figure 20 indicates that baroclinic torques tend to strengthen the vorticity of the bottom row at the expense of the top row.

Thus, density variation plays two different roles in the development of the three-dimensional form of the layer. At the early stages, it generates an asymmetric strain field by imparting a convective motion to the core. At the later stages, it redistributes the vorticity within the core. The development of the instability modes in the variable-density shear layer highlights the importance of the asymmetry of the flow and strain fields. In the interpretation of the origin of the complicated structures associated with the three-dimensional effects, the influence of strain and density gradient, which are respectively taken into account in the equation of motion through the vorticity stretching and baroclinic production terms, may be hard to distinguish in the results. To facilitate this task, we consider the case of a uniform-density shear layer with an asymmetric vorticity distribution at $t = 0$, and postpone further discussion until the results are analysed.

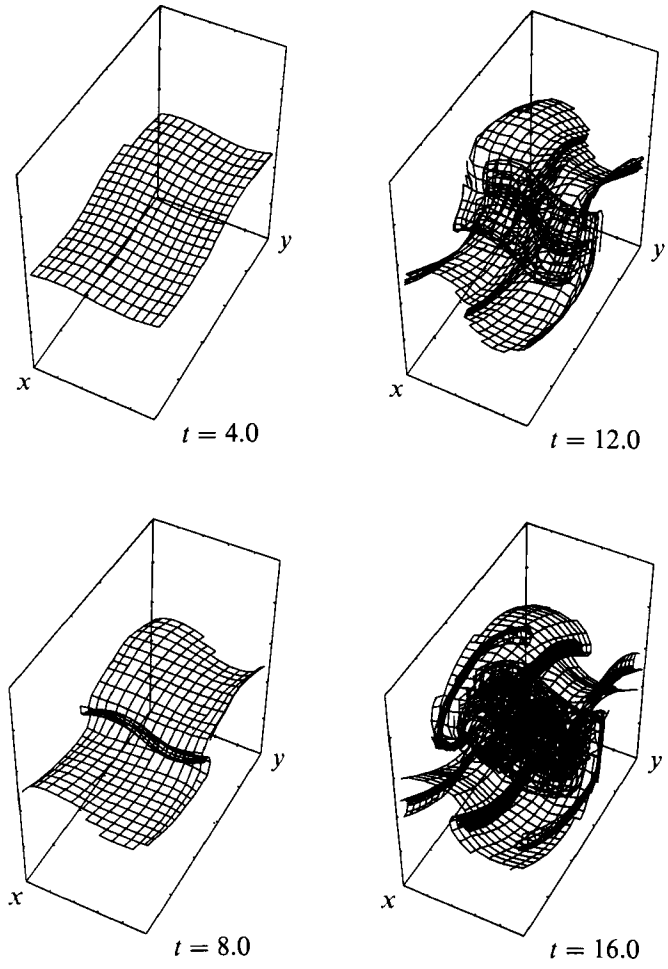

FIGURE 21. Three dimensional perspective view of the surface $s = 0$, initially lying in the plane $z = 0$ for the shear layer with an initially asymmetric vorticity. The plots were generated from the point of view of an observer located at (48, 24, 48).

3.3. *Uniform-density asymmetric shear layer*

Shear layers with asymmetric vorticity profiles are frequently encountered. Typically, these layers are formed following the merging, downstream of the splitter plates, of boundary layers of unequal thicknesses and opposite sign of vorticity. The velocity profile associated with the asymmetric vorticity distribution thus produced can be modelled as the superposition of a symmetric velocity profile induced by an idealized symmetric vorticity distribution, and a wake component biased towards the low-velocity stream. As shown by Koochesfahani & Frieler (1989), the wake component becomes important when the density of the slow stream is much larger than that of the fast stream. In such instances, linear stability analysis shows that the early development of the layer is dominated by the wake mode whose amplification rate is higher than that of the shear-layer mode. In the remaining cases, the shear-layer mode is dominant, and leads to the familiar rollup of the Kelvin–Helmholtz waves.

While the wake component might be neglected in two-dimensional models, results of Ashurst & Meiburg (1988) have shown that the detail of the vorticity distribution

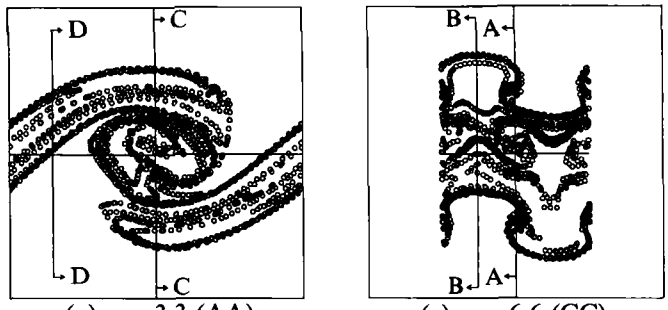

(*a*) $y = 3.3$ (AA) (*c*) $x = 6.6$ (CC)

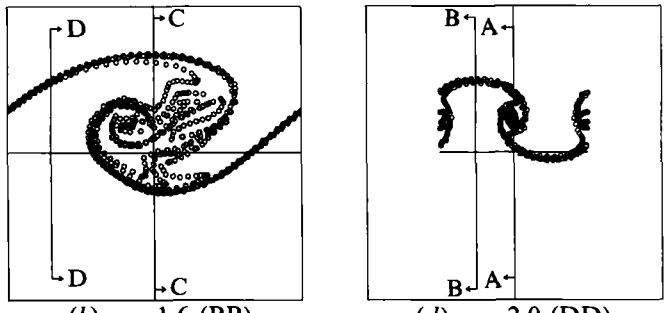

(*b*) $y = 1.6$ (BB) (*d*) $x = 2.0$ (DD)

FIGURE 22. Intersection of the Lagrangian mesh at $t = 16.0$ with the planes defined by (*a*) $y = 3.3$, (*b*) $y = 1.6$, (*c*) $x = 6.6$, and (*d*) $x = 2.0$.

Material layer	z location	$t = 4.0$		$t = 8.0$		$t = 12.0$		$t = 16.0$	
		A	N	A	N	A	N	A	N
1	−1.32	1.03	1.00	1.14	1.20	1.72	1.69	3.54	4.16
2	−0.66	1.04	1.00	1.24	1.33	2.40	2.54	5.31	8.55
3	0	1.04	1.00	1.44	1.44	2.78	3.51	5.87	9.95
4	0.66	1.04	1.00	1.22	1.31	2.36	2.48	5.01	7.35
5	1.32	1.03	1.00	1.11	1.15	1.56	1.73	3.38	3.91

TABLE 3. Normalized surface area, A, and number of elements, N, for the individual material layers

plays an important role in the development of three-dimensional instability modes. Using two vorticity layers of opposite sign, they predicted an asymmetric spacing of the streamwise vortex rods similar to that experimentally observed (Lasheras & Choi 1988). However, this approach is complicated by the difficulty in specifying the initial strength and separation of the vorticity layers. In fact, the initial separation of the individual vorticity layers is not uniquely determined in that model, and large separation distances may lead to the independent rollup of each layer, a behaviour that is not obtained in shear layers.

In our study, consideration of shear layers with asymmetric vorticity profiles is motivated by the results of the variable-density layer. In particular, the numerical experiment is designed to mimic the early effects of density variation which were shown to promote the spanwise vorticity of the low-density stream at the expense of that on the high-density side through asymmetric strain. This imitation is obtained by perturbing the second-order Gaussian vorticity profile to yield the asymmetric vorticity distribution shown by a broken line in figure 1. A single vorticity layer in

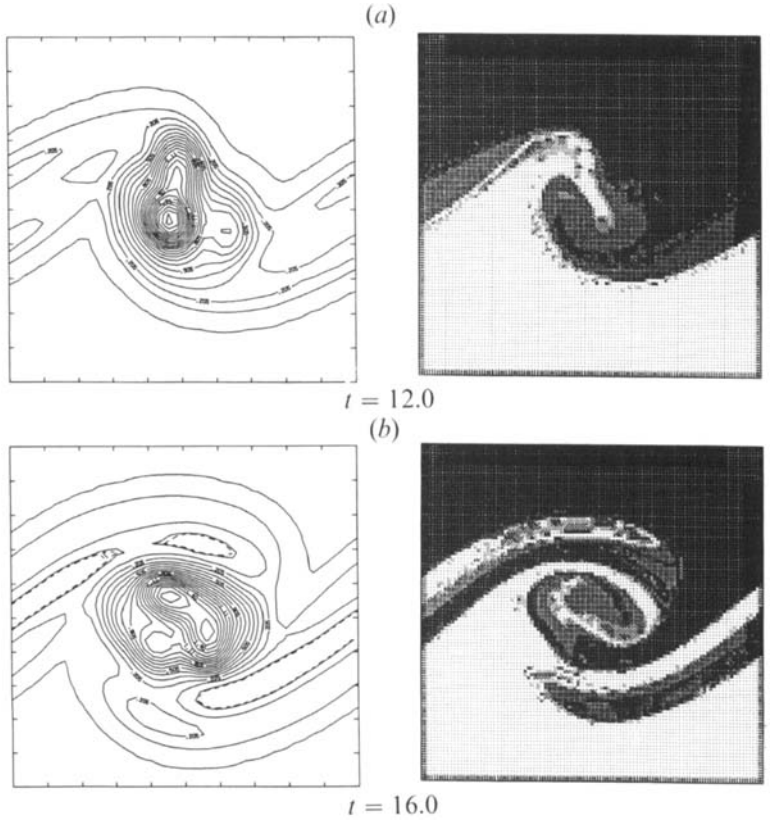

FIGURE 23. Spanwise vorticity, ω_y, (left) and scalar contours (right) plotted in the plane $y = 3.3$.

which the velocity increases monotonically from one stream to the other is considered. The scalar is assumed passive, and its initial profile is the same as that used in §3.1. We keep the same dimensions and boundary conditions, and apply the same perturbation at the start of the computations. Since the deviation from the symmetric Gaussian profile is small, we expect similar growth characteristics of the two-dimensional component of the perturbation, although its wavelength may not correspond to that of the most amplified Kelvin–Helmholtz mode.

3.3.1. *Deformation of material surfaces*

Perspective views of the material surface initially lying in the plane $z = 0$, shown in figure 21, exhibit qualitative similarity to that of the first case and hence a detailed analysis of the Lagrangian motion is omitted. Our discussion will be restricted to the features by which the asymmetric layer may be identified. The deformation of the material layers is asymmetric with respect to the surface initially at $z = 0$, as indicated in table 3. This development resembles that observed in the variable-density case where baroclinic vorticity generation produces a similar asymmetric strain field. Despite this similarity, the two cases can be distinguished by the fact that, in the asymmetric uniform-density layer, the core does not exhibit any convective motion. The cross-sections of the material surfaces, plotted in figure 22, show that the asymmetry is primarily exhibited in the core where the top and bottom mushrooms are distinguishable. However, unlike the previous case, there is no indication that they have different strengths.

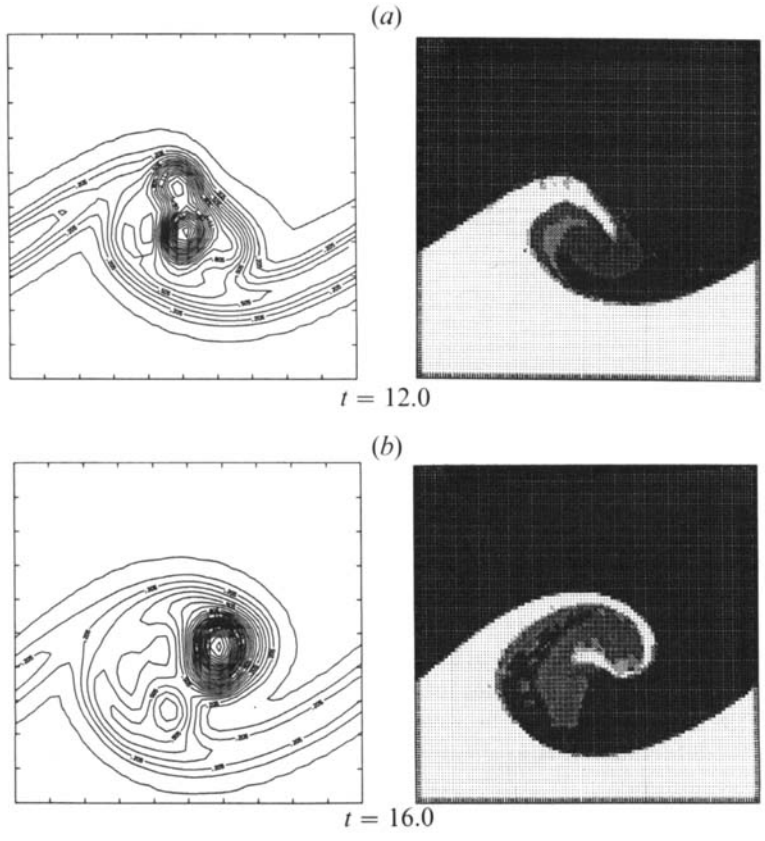

FIGURE 24. Spanwise vorticity, ω_y (left) and scalar contours (right) plotted in the plane $y = 5.0$.

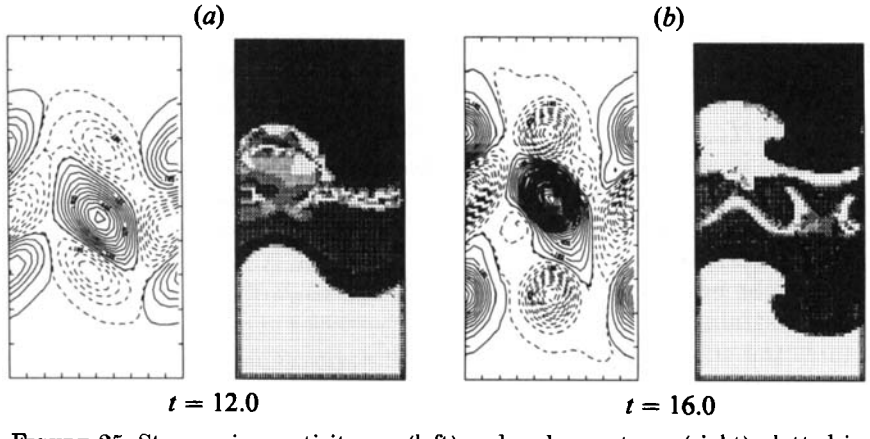

FIGURE 25. Streamwise vorticity, ω_y (left) and scalar contours (right) plotted in the plane $x = 6.6$.

3.3.2. *Vorticity and scalar distribution*

Figures 23–26 show scalar and vorticity contours plotted in the nonlinear stages of evolution of the flow, $t = 12.0$ and 16.0. The spanwise sections show that some but not all the effects associated with density variation exist in this case. While the convective motion could not be captured, the vorticity and scalar distributions

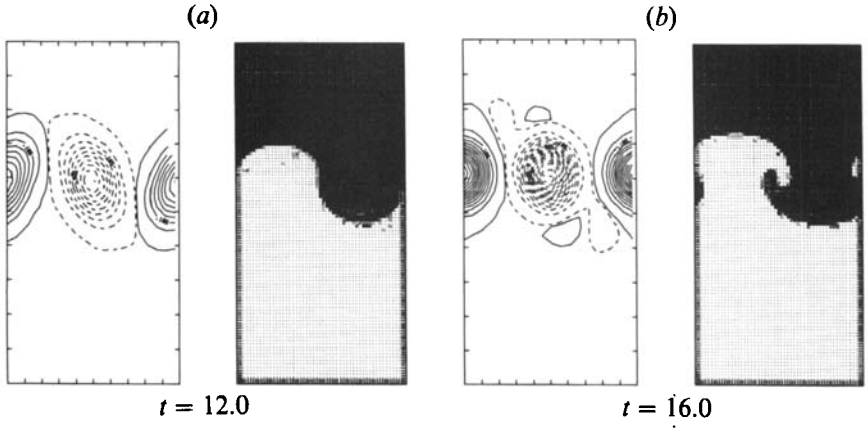

FIGURE 26. Streamwise vorticity, ω_y (left) and scalar contours (right) plotted in the plane $x = 2.0$.

exhibit weak asymmetry at all spanwise cuts, and the rotation of the core resembles the eccentric rotation of an oval-shaped body. Asymmetric entrainment patterns, whereby more fluid from the bottom stream reaches the core, are also established. At $t = 16.0$, the composition of the eddy slightly favours bottom-layer fluid, as the net entrainment ratios admit small deviations from unity, $(S_{3D})^-/(S_{3D})^+ = 1.026$, and $(S'_{3D})^-/(S'_{3D})^+ = 1.037$. This corroborates our discussion of the motion of the material surfaces, whose deformation is found to be more severe in the bottom stream. On the other hand, the similarity between the asymmetric and variable-density layers is restricted to the fact that these layers can be identified by larger spanwise vorticity values.

The spinning of the asymmetric spanwise eddy causes the generation of streamwise vortex rods of different strengths as they approach the core. Unlike the variable-density case, the vortex rods on the bottom side are intensified at a lower rate in the early stages, $t < 12.0$, and this effect is reversed at the later stages. At $t = 12.0$, the ratio of the circulation of the two streamwise vortices is $\Gamma_{top}/\Gamma_{bot} = 1.313$, and decreases to $\Gamma_{top}/\Gamma_{bot} = 0.982$ at $t = 16.0$. This asymmetry occurs mainly as a result of the difference in shape and size of the streamwise rods as the maximum vorticity values in both remain close. A simplified model clarifying the origin of the difference in strengths between the streamwise rods can be constructed by noting that the stretching of the streamwise vorticity occurs along the streamwise boundaries of the domain where the braids are anchored and pulled towards the core of the eddy. In the braids, the strain is weakly dependent on the detail of the distribution within the core. In fact, the strain in the braids may be approximated by concentrating the spanwise vorticity of the core along its centre. Thus, the asymmetry of the vorticity distribution of the spanwise core and of its induced flow and strain fields, are not expected to play a major role in the production of streamwise vorticity. The observed asymmetry becomes essentially a consequence of the eccentric spinning of the spanwise cores.

In the variable-density layer, the above description is modified by the baroclinic production of vorticity. The streamwise component of the baroclinic torque, τ_x, is small in the braids, so that the production of streamwise vorticity there is dominated by strain and the contribution of the baroclinic torque to the strength of the streamwise vortices only appears as a modulation of the local vorticity values. On the

other hand, τ_x increases significantly as we approach the core. Focusing on the later stages of the flow, this observation is justified by realizing that fluid acceleration, which controls the production of baroclinic vorticity, becomes dominated by the convective acceleration. In turn, the convective acceleration must be larger in regions of higher curvature. Therefore, in the variable-density layer, as the streamwise vortices approach the core, their strengths are affected by the baroclinic source term which is shown to strengthen (weaken) the streamwise vorticity of the vortex rods lying on the low-density (high-density) side.

Our numerical results have shown that three mechanisms can lead to symmetry loss in three-dimensional temporal shear layers. The first is associated with the growth of the translative instability which leads to a preferential entrainment pattern reversing itself every half spanwise wavelength of the instability. The second is caused by an initially asymmetric vorticity distribution which induces asymmetric entrainment currents favouring the free stream having higher spanwise vorticity values. Finally, baroclinic vorticity generation plays an important role in the formation of asymmetric structures by imparting a convective motion on the cores and redistributing the vorticity within the cores. These mechanisms should be distinguished from similar effects occurring in two- and three-dimensional spatially developing layers, in which individual mechanisms may be hard to isolate since asymmetric entrainment favouring the high-speed stream is observed before the transition to three-dimensional motion, and the location of vortex amalgamation, which lead to the formation of composite structures of even higher complexity, is not easily predicted (Dimotakis 1986).

The use of asymmetric vorticity distribution, with a strong negative component, has been suggested by Ashurst & Meiburg (1988) as a means of simulating the effect of the velocity ratio. Their computations were able to capture the asymmetric spacing of the streamwise vortices, observed experimentally by Lasheras & Choi (1988). This asymmetric spacing was not observed in our computations which did not include a negative initial vorticity component. Thus, we conclude that the presence of negative vorticity alone cannot be responsible for this effect and the asymmetric spacing of the streamwise vortices is not a property of the 'primary' three-dimensional structure. However, the development described by Ashurst & Meiburg (1988) could occur during the merging of the distorted spanwise eddies. In view of the results of Metcalfe *et al.* (1987), who showed that in the absence of pairing, both two- and three-dimensional instabilities tend to saturate, the suggestion that the asymmetric spacing is a product of a higher-order instability could be justified. This interpretation is consistent with the experimental findings of Bernal & Roshko (1986), and with the numerical simulations of Grinstein *et al.* (1989), who observed that an asymmetric reorganization of the streamwise vortices occurs after the merging of the distorted spanwise eddies.

4. Conclusions

The transport element method was applied to study the evolution of temporal, doubly periodic, uniform- and variable-density shear layers. The numerical schemes are Lagrangian and adaptive. They are based on tracking the vorticity, scalar and scalar gradients, discretized using a finite number of computational elements. Three cases are considered: (i) a uniform-density vorticity layer with symmetric vorticity profile, (ii) a variable-density vorticity layer, and (iii) a uniform-density asymmetric layer. In the uniform-density case, we take advantage of Kelvin's circulation

theorem in order to save computational effort, while the vorticity transport equation is used when the baroclinic source term is present. Thus, the vortex stretching is implicitly taken into account in the first case, while direct evaluation of the vorticity stretching and baroclinic source terms is performed in the second.

Starting from equal 'small-amplitude' two- and three-dimensional perturbations, the evolution of the vorticity layer first exhibits a two-dimensional regime which is characterized by the growth and rollup of the Kelvin–Helmholtz mode. Following this stage, three-dimensional perturbations are rapidly amplified. In all cases, and consistent with previous results, two types of three-dimensional instability are observed: an instability in the braids which leads to the formation of streamwise vortex rods and scalar mushroom structures, and a core instability which causes an uneven deformation of the spanwise eddies. The instability in the braids is associated with the severe stretching of the vortex lines whose extension in the streamwise direction exceeds the separation distance between neighbouring spanwise eddies. The streamwise vortex rods are continuously wrapped around the deformed spanwise cores leading to the intensification of the streamwise and spanwise components of vorticity and to the generation of complex vortex structures. While the amplitude of instability of the spanwise eddies does not reach such large values, it is still found to play an important role in the evolution of the flow field.

A detailed visualization of the vorticity and scalar fields and of the motion of material surfaces was performed. The study focuses on the manifestation of three-dimensional instabilities in vorticity layers. The three-dimensional instability in a vorticity layer with initially symmetric vorticity and scalar profiles exhibits asymmetric vorticity and scalar distributions at different spanwise locations. These forms of asymmetry, which reverse themselves every one-half spanwise periodicity length, are linked to the development of the braids and translative instabilities. Similar entrainment currents are observed in a uniform-density asymmetric vorticity layer, where the asymmetry of the flow field leads to a preferential entrainment of irrotational fluid from the stream initially having higher spanwise vorticity values. In this case, the effect of the asymmetric vorticity distribution combines with that of the three-dimensional instability, whose development is not significantly altered from the previous case, resulting in a net departure from a unity entrainment ratio. The variable-density layer is identified by a finite convective speed of the eddies in the direction of the high-density fluid stream and by an asymmetric entrainment pattern favouring the low-density stream. Baroclinic torques affect the development of the three-dimensional modes via uneven intensification or weakening of the streamwise vorticity.

Special attention was paid to the evolution of the unstable modes, and on their roles in reorganizing the flow field. We were thus content to observe unstable modes given by a single spanwise wavelength, which was chosen close to the most amplified mode of the linear stability theory. We leave to a subsequent study the task of trying to determine the characteristics of the processes which lead to the wavelength selection of the three-dimensional modes. Moreover, we have restricted our study to the formation and maturation of the primary three-dimensional structures. We have thus omitted the pairing interactions between these structures and their role in the mixing transition and growth of the layer. These computations are currently being considered.

This work is supported by the Air Force Office of Scientific Research Grant AFOSR 84-0356, the National Science Foundation Grant CBT-8709465, and the

Department of Energy Grant DE-FG04-87AL44875. Computer support is provided by the John von Neumann National Supercomputer Center.

REFERENCES

ASHURST, W. T. & MEIBURG, E. 1988 *J. Fluid Mech.* **189**, 87.

BATCHELOR, G. K. 1967 *An Introduction to Fluid Dynamics.* Cambridge University Press.

BEALE, J. T. 1986 *Math. Comput.* **46**, 401.

BEALE, J. T. & MAJDA, A. 1982*a* *Math. Comput.* **39**, 1.

BEALE, J. T. & MAJDA, A. 1982*b* *Math. Comput.* **39**, 29.

BEALE, J. T. & MAJDA, A. 1985 *J. Comput. Phys.* **58**, 188.

BERNAL, L. P. 1981 The coherent structure of turbulent mixing layers. Ph.D. thesis, California Institute of Technology.

BERNAL, L. P. & ROSHKO, A. 1986 *J. Fluid Mech.* **170**, 499.

BREIDENTHAL, R. 1980 *Phys. Fluids* **23**, 1929.

BREIDENTHAL, R. 1981 *J. Fluid Mech.* **109**, 1.

BROWAND, F. K. & TROUTT, T. R. 1980 *J. Fluid Mech.* **97**, 771.

BROWN, G. L. & ROSHKO, A. 1974 *J. Fluid Mech.* **64**, 775.

CHORIN, A. J. 1973 *J. Fluid Mech.* **57**, 785.

CORCOS, G. M. & LIN, S. J. 1984 *J. Fluid Mech.* **139**, 67.

CROW, S. C. & CHAMPAGNE, F. H. 1970 *J. Fluid Mech.* **48**, 547.

DIMOTAKIS, P. E. 1986 *AIAA J.* **24**, 1791.

DIMOTAKIS, P. E. 1989 *AIAA Paper* 89-0262.

GHONIEM, A. F., HEIDARINEJAD, G. & KRISHNAN, A. 1988 *J. Comput. Phys.* **79**, 135.

GHONIEM, A. F. & KRISHNAN, A. 1988 In *Twenty-Second Symp. (Intl) on Combustion*, p. 665. The Combustion Institute.

GREENGARD, C. 1986 *Math. Comput.* **47**, 387.

GRINSTEIN, F. F., HUSSAIN, F. & ORAN, E. S. 1989 *AIAA Paper* 89-0977.

HO, C.-H. & HUERRE, P. 1984 *Ann. Rev. Fluid Mech.* **16**, 365.

HUSSAIN, A. K. M. F. 1986 *J. Fluid Mech.* **173**, 303.

INOUE, O. 1989 *AIAA J.* **27**, 1517.

JIMENEZ, J. 1983 *J. Fluid Mech.* **132**, 319.

JIMENEZ, J., COGOLLOS, M. & BERNAL, L. P. 1985 *J. Fluid Mech.* **152**, 125.

KNIO, O. M. & GHONIEM, A. F. 1988 *AIAA Paper* 88-0728.

KNIO, O. M. & GHONIEM, A. F. 1990 *J. Comput. Phys.* **86**, 75.

KNIO, O. M. & GHONIEM, A. F. 1991 *J. Comput. Phys.* **97**, 172.

KNIO, O. M. & GHONIEM, A. F. 1992 *AIAA J.* **30**, 105.

KONRAD, J. H. 1976 An experimental investigation of mixing in two-dimensional turbulent shear flows with applications to diffusion-limited chemical reactions. Ph.D. thesis, California Institute of Technology.

KOOCHESFAHANI, M. M. & FRIELER, C. E. 1989 *AIAA J.* **27**, 1735.

KOOP, C. G. & BROWAND, F. K. 1979 *J. Fluid Mech.* **93**, 135.

KRISHNAN, A. 1989 Numerical study of vorticity-combustion interactions in shear flow. Ph.D. thesis, MIT.

LASHERAS, J. C., CHO, J. S. & MAXWORTHY, T. 1986 *J. Fluid Mech.* **172**, 231.

LASHERAS, J. C. & CHOI, H. 1988 *J. Fluid Mech.* **189**, 53.

LEONARD, A. 1985 *Ann. Rev. Fluid Mech.* **17**, 525.

LIN, S. J. & CORCOS, G. M. 1984 *J. Fluid Mech.* **141**, 139.

LOWERY, P. S., REYNOLDS, W. C. & MANSOUR, N. N. 1987 *AIAA Paper* 87-0132.

MAJDA, A. & SETHIAN, J. A. 1987 *Combust. Sci. Tech.* **42**, 185.

MASLOWE, S. A. & KELLY, R. E. 1971 *J. Fluid Mech.* **48**, 405.

McMurtry, P. A., Riley, J. J. & Metcalfe, R. W. 1989 *J. Fluid Mech.* **199**, 297.

Metcalfe, R. W., Orszag, S. A., Brachet, M. E., Menon, S. & Riley, J. J. 1987 *J. Fluid Mech.* **184**, 207.

Neu, J. C. 1984 *J. Fluid Mech.* **143**, 253.

Pierrehumbert, R. T. & Widnall, S. E. 1982 *J. Fluid Mech.* **114**, 59.

Rehm, R. G. & Baum, H. R. 1978 *J. Res. Natl Bur. Stand.* **83**, 297.

Riley, J. J. & McMurtry, P. A. 1989 In *Turbulent Reactive Flows* (ed. R. Borghi & S. N. B. Murthy), p. 486. Springer.

Widnall, S. E. & Tsai, C.-Y. 1977 *Proc. R. Soc. Lond.* A **287**, 273.

Winant, C. D. & Browand, F. K. 1974 *J. Fluid Mech.* **41**, 327.

Wygnanski, I., Oster, D., Fiedler, H. & Dziomba, B. 1979 *J. Fluid Mech.* **93**, 325.